PAPER • **OPEN ACCESS**

Nanosecond-pulsed volume DBD plasma in saturated humid air: a combined experimental and computational study using EFISH and LIF

To cite this article: Lorenzo Ibba *et al* 2025 *Plasma Sources Sci. Technol.* **34** 105012

OPEN ACCESS
IOP Publishing
Plasma Sources Science and Technology
Plasma Sources Sci. Technol. **34** (2025) 105012 (21pp)
https://doi.org/10.1088/1361-6595/ae0765

Nanosecond-pulsed volume DBD plasma in saturated humid air: a combined experimental and computational study using EFISH and LIF

Lorenzo Ibba[1,*], Giacomo Pierotti[2], Arturo Popoli[2], Domenico Aceto[3], Carlos D Pintassilgo[4,5], Andrea Cristofolini[2], Paolo F Ambrico[3] and Ivo Furno[1]

[1] Ecole Polytechnique Fédérale de Lausanne (EPFL), Swiss Plasma Center (SPC), CH-1015 Lausanne, Switzerland
[2] Department of Electrical, Electronic and Information Engineering "Guglielmo Marconi", University of Bologna, Viale Risorgimento 2, 40134 Bologna, Italy
[3] CNR, Istituto per la Scienza e Tecnologia dei Plasmi, Sede di Bari, c/o Dipartimento di Fisica, Campus Universitario, Via Amendola 173, Bari, Italy
[4] Faculdade de Engenharia, Universidade do Porto, R. Dr Roberto Frias, 4200–465 Porto, Portugal
[5] Instituto de Plasmas e Fusão Nuclear, Instituto Superior Técnico, Universidade de Lisboa, 1049-001 Lisboa, Portugal

E-mail: lorenzo.ibba@outlook.com

Received 27 May 2025, revised 4 September 2025
Accepted for publication 16 September 2025
Published 13 October 2025

Abstract

This study presents a detailed investigation of a nanosecond-pulsed volume dielectric barrier discharge (VDBD) plasma in saturated humid air at atmospheric pressure, combining experimental diagnostics with kinetic modeling. Electric field-induced second harmonic generation (EFISH), employing a spatial filter and a picosecond laser, enabled electric field measurements with high spatial (270 μm) and temporal (28 ps) resolution at three distinct positions across the inter-electrode VDBD gap. These measurements revealed previously unobserved features and consistent differences between the discharge center and regions near the ground and high-voltage (HV) electrodes. Near the ground electrode, a higher electric field was observed prior to the first positive plasma discharge, along with an overshoot up to 50 kV cm^{-1} during plasma breakdown, absent at the center and near the HV electrode. A sharper post-breakdown decrease and recovery in the electric field was also observed near the ground electrode, differently from the other positions. This pattern inverted during the subsequent negative discharge at the end of the HV pulse, with the higher electric field being measured near the HV electrode. To complement the electric field data, the concentrations of

* Author to whom any correspondence should be addressed.

nitric oxide (NO) and hydroxyl radical (OH) were measured using laser-induced fluorescence (LIF), providing insight into their temporal dynamics during and after the discharge. The EFISH data served as input for a zero-dimensional kinetic model, which revealed the dynamics of both charged and neutral species, showing excellent agreement with the LIF data and validating the model accuracy. The simulation identified OH^-, O_2^-, and O_4^- as the key negative ions responsible for the stable electric field after plasma breakdown. This research highlights the importance of understanding electric field dynamics and reactive species formation in low-temperature plasmas. Integrating EFISH and LIF data with kinetic modeling provides a robust framework to optimize plasma-based systems, improving their performance and safety in practical applications.

Keywords: low temperature plasma, electric field-induced second harmonic generation (EFISH), laser-induced fluorescence (LIF), kinetic modeling, picosecond EFISH, nanosecond-pulsed volume dielectric barrier discharge (VDBD), atmospheric pressure plasmas

1. Introduction

Low-temperature plasmas (LTPs) at atmospheric pressure are extensively studied for a wide range of biological applications [1, 2]. Their potential in various fields, including plasma agriculture [3–6], food processing [7, 8], plasma medicine [9–16], and disinfection and sterilization [17–28], has attracted significant attention. A deeper understanding of atmospheric pressure plasmas in humid air is crucial to elucidate the mechanisms of plasma-biological interactions in practical applications. Such knowledge will help identify which plasma products are beneficial for specific applications and which may be harmful, thereby enabling the optimization of plasma sources for improved safety and performance.

To better understand the dynamics of charged particles in the plasma, electric field measurements are crucial, as the electric field is directly linked to particle kinetics and, consequently, to plasma chemistry. A recently developed advanced laser technique, known as electric field-induced second harmonic generation (EFISH), now enables the measurement of electric fields with exceptionally high spatial and temporal resolution. Enabled by the recent use of ultrashort laser pulses [29, 30], EFISH measurements have gained increasing prominence in diverse plasma applications, including ionization wave plasmas in air, nitrogen, hydrogen, and hydrocarbon flames, as well as argon and helium plasma jets [29, 31–33]. These measurements provide valuable insights into the dynamics of ions and electrons during both plasma breakdown and the entire discharge process. A previous study probed the electric field at various positions within the plasma discharge volume but found no differences between the central region and the areas near the dielectric surfaces, contrary to the expectations of kinetic models [34]. This discrepancy was likely due to the limited spatial resolution imposed by the width of the laser beam. In this work, we measure the electric field evolution during the plasma discharge using the picosecond laser EFISH method, with improved spatial and temporal resolution to gain deeper insight into the plasma breakdown. Additionally, EFISH measurements are extremely useful for the implementation and refinement of kinetic models. The electric field measurements have already been used for the validation of simple kinetic models [34], however, using the electric field as input can deliver more robust simulations and consequently yield better predictions.

Kinetic models play a vital role in the prediction of plasma behavior and the identification of the chemical pathways activated under different conditions, such as air composition, humidity levels, and device configuration. Different kinetic models for atmospheric pressure plasmas in air can be found in the literature, referring to different plasma sources such as DC discharges [35], corona discharges [36], surface DBDs [37–39] and volumetric DBDs [40, 41]. To simulate in detail the complex kinetics of air plasmas, hundreds of species and thousands of reaction paths with extremely different characteristic timescales are usually needed [42–44]. For this reason, multidimensional models (commonly the drift-diffusion models, e.g. [45, 46]) can hardly be used to simulate long time intervals. In this spirit, zero-dimensional (0D) models (also known as global models) are usually employed to focus on the complex chemistry of air plasmas while maintaining an acceptable computational effort. Global models are fundamentally based on solving a set of coupled differential equations that describe the time evolution of the chemical species under consideration. A critical aspect of these models is to provide a realistic estimate of the reduced electric field, $E(t)/N$, over time, as many physical and chemical processes are highly sensitive to this parameter. Consequently, users of global models typically employ one of the following approaches to estimate $E(t)/N$:

- Calculate $E(t)/N$ (and, if necessary, the electron number density) by ensuring consistency with the experimentally measured electrical power absorbed by the device [42, 47].
- Use an equivalent electric circuit approach (see, e.g. [41, 48]) to derive $E(t)/N$ from the applied voltage $v(t)$.
- Incorporate experimental data directly describing the behavior of the electric field, as implemented in this work.

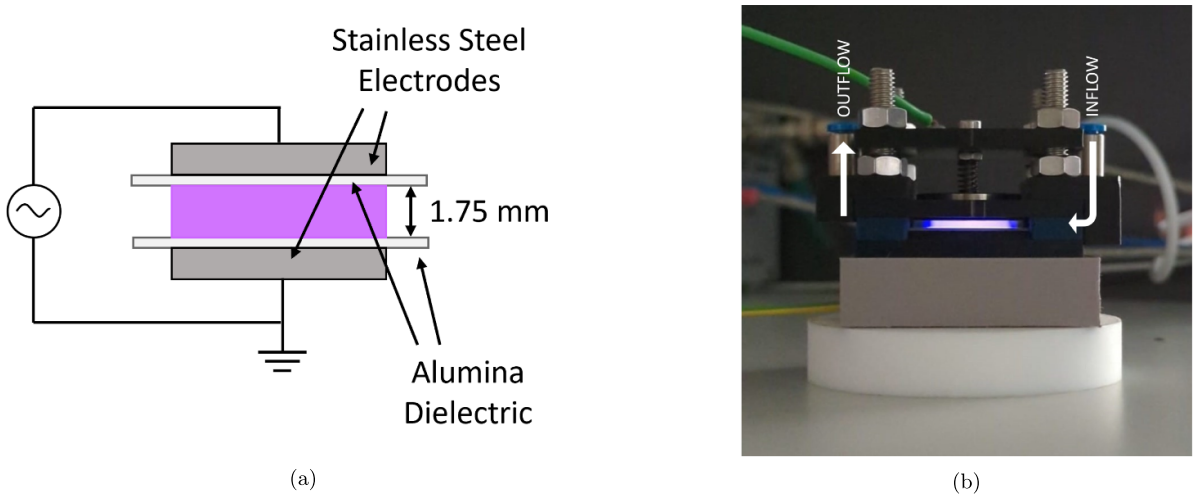

Figure 1. (a) Schematic of the VDBD components. (b) Picture of the operating VDBD with the schematics of the inflow and outflow positions.

In the present study, the electric field measured by EFISH is incorporated into a 0D kinetic model, which is then used to predict the dynamics of relevant molecules and reactive species, such as NO and OH, produced in the plasma volume. Finally, the absolute density of NO and the relative density of OH are measured using laser-induced fluorescence (LIF) to show the kinetics of these two molecules, relevant for multiple biological applications, as well as to validate the results of the kinetic model and show the robustness of the code.

The paper is organized as follows. Section 2 provides a description of the plasma source and operating parameters. A detailed overview of the materials and methods used for the EFISH and LIF diagnostic techniques is presented in sections 3 and 4, along with the corresponding experimental results in section 5. The kinetic modeling framework is presented in section 6, and the simulation results are discussed in comparison with the experimental data in section 7. Finally, the main conclusions of this work are presented in section 8.

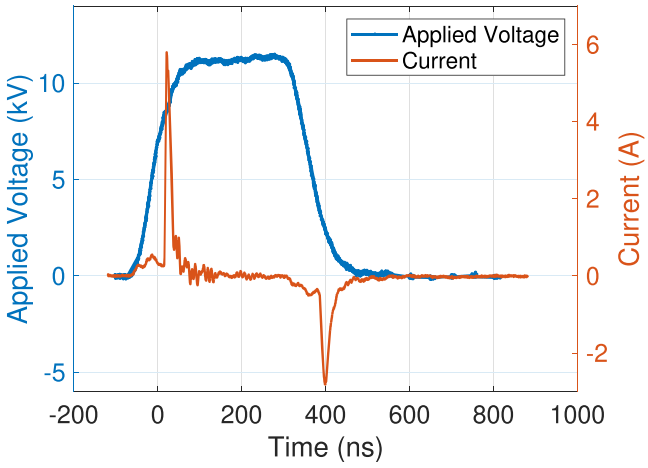

Figure 2. Voltage waveform and current measured on the VDBD electrodes. The current peaks indicate the two plasma discharges, the first positive, and the second negative.

2. Nanosecond-pulsed volume DBD

The plasma discharge is generated using a volume dielectric barrier discharge (VDBD) driven by a custom-built nanosecond-pulsed high-voltage (HV) power supply [49], capable of producing monopolar pulses as short as 200 ns, with peak voltages up to 25 kV, at repetition frequencies ranging from 100 to 2000 Hz. The VDBD setup consists of a plate-to-plate round electrode geometry, identical to the configuration described in [34].

The electrodes are circular stainless steel brass plates, each 20 mm in diameter, and are coated with 0.668 mm thick CoorsTek 99.5% alumina (Al_2O_3) ceramic plates, which serve as dielectric barriers, as illustrated in the schematic in figure 1(a). To maintain consistency between the experimental setup and the simulation, both the applied voltage and the gas flow configuration are kept constant throughout each diagnostic.

The VDBD is operated with a monopolar 200 ns HV pulse at approximately 11.6 kV, with a repetition frequency of 1 kHz, and a rise/fall time of approximately 50 ns, as shown in figure 2. The measured current, also shown in figure 2, indicates the occurrence of two plasma discharges, in correspondence of the two peaks, the first positive and the second negative. From this point forward, the term positive plasma discharge refers to the first plasma discharge, and negative plasma discharge refers to the second discharge at the end of the HV pulse. The gas flow is precisely controlled using a Bronkhorst mass flow controller, which regulates the supply of dry synthetic air (80%/20% N_2/O_2). This air is introduced into a 500 cc glass bubbler containing deionized water to produce saturated humid synthetic air. The flow rate is set at 1000 sccm of saturated humid air, which is directed into the VDBD gap, as illustrated in figure 1(b). Assuming a closed system, at this flow rate and a plasma frequency of 1 kHz,

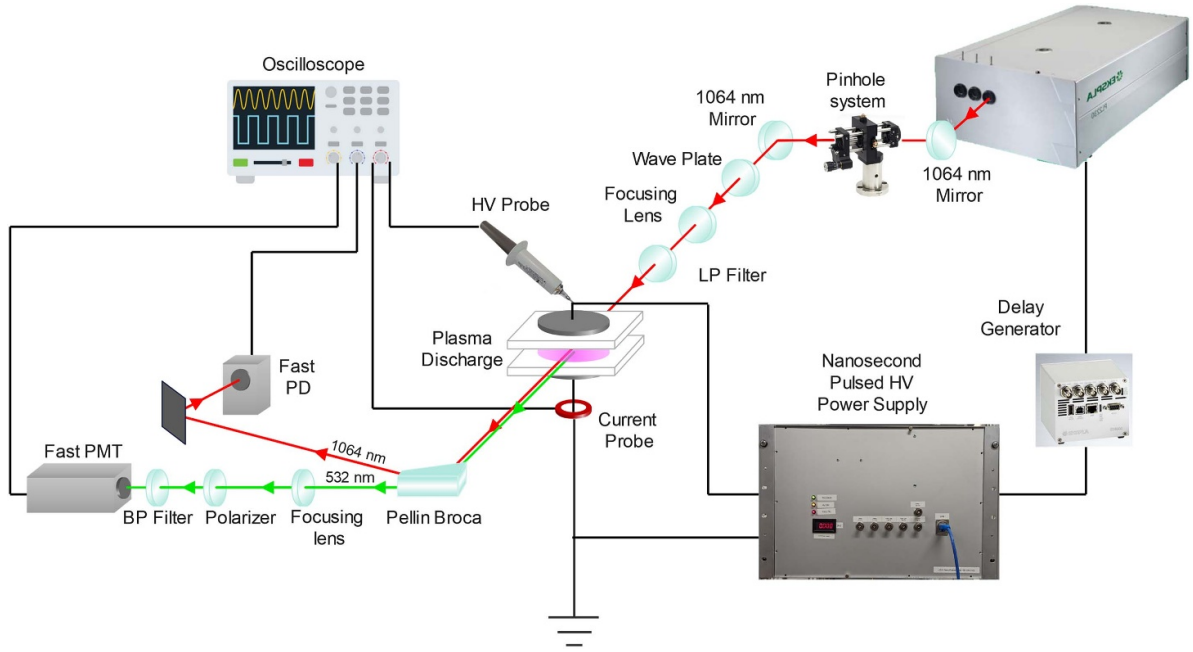

Figure 3. Experimental setup schematics used for the EFISH measurements.

each gas portion is exposed to approximately 33 HV pulses. Finally, the homogeneity and diffuse nature of the plasma in this particular setup, which is essential for the validity of the EFISH measurements, has already been demonstrated in [34].

3. EFISH experimental setup

To perform the EFISH measurements, a diode-pumped high-energy picosecond Nd:YAG laser (PL2231-50 EKSPLA) was employed. This laser system consists of a diode-pumped solid-state master oscillator, passively generating high repetition rate pulse trains at 87 MHz. The output energy of the 1064 nm fundamental beam reaches up to 30 mJ, with a pulse duration of ∼28 ps and a pulse frequency of 50 Hz. The schematic of the experimental setup used for the EFISH measurements is reported in figure 3.

The fundamental 1064 nm output of the picosecond laser is directed to a spatial filter using Nd:YAG dual-order laser mirrors (Thorlabs NB1-K13), which are designed to accommodate both the fundamental (1064 nm) and the second harmonic (532 nm) for alignment purposes. The spatial filter consists of a 75 μm diameter stainless steel pinhole (Thorlabs P75K) and 25 mm N-BK7 aspheric lenses with a focal length of 50 mm (Thorlabs AL2550-C) to focus the beam into the pinhole. This setup improves the Gaussian beam quality and reduces the beam size close to the focus point, thereby enhancing spatial resolution and allowing the laser beam to approach the dielectric surface without clipping on the sides of the VDBD. After passing through the spatial filter, the laser beam is guided between the two parallel circular electrodes of the VDBD. The polarization plane of the laser is initially vertical. However, for fine adjustments and to correct small alignment errors, a polymer zero-order half-wave plate (Thorlabs WPH10E-1064) mounted on a rotation stage is used. Stray second harmonic signals generated within the focusing lens, as well as residual signals from the laser optical parametric generator, are blocked using an 850 nm long-pass (LP) filter (Thorlabs FGL850M). A 50 cm focal length lens is employed to focus the laser beam between the electrodes, as depicted in figure 3. The VDBD is placed on a motorized high-load vertical translation stage (Thorlabs MLJ150/M), allowing for precise control of the laser beam vertical position within the plasma discharge with an accuracy of 10 μm. On top of the vertical translation stage, an horizontal micrometer translation stage is used to precisely position the laser beam at the horizontal center of the VDBD. After traversing the electrode gap, the laser beam contains both the second harmonic signal at 532 nm, generated by the electric field between the electrodes, and the fundamental 1064 nm pump beam. A Pellin Broca prism (Thorlabs ADBU-10) is used to separate the second harmonic beam from the pump beam, which is subsequently refocused and detected by a photomultiplier tube (PMT) (Hamamatsu Fast PMT, model H10721-20, nominal rise time of 0.57 ns). To isolate the vertically polarized EFISH signal, which originates from the vertical electric field component between the electrodes, a thin-film polarizer (Thorlabs PVISE050-A) mounted on a rotation stage is positioned before the PMT. A narrow band-pass (BP) filter (Thorlabs FL532-10, CWL $= 532 \pm 2$ nm, FWHM $= 10 \pm 2$ nm) is placed in front of the PMT to block stray light and reflections from the fundamental harmonic. The PMT gain is set at 0.6 V to ensure linearity across the entire range of the measured electric field. A fast photodiode (PD) (Thorlabs DET10A2) is used to detect a reflection of the 1064 nm beam.

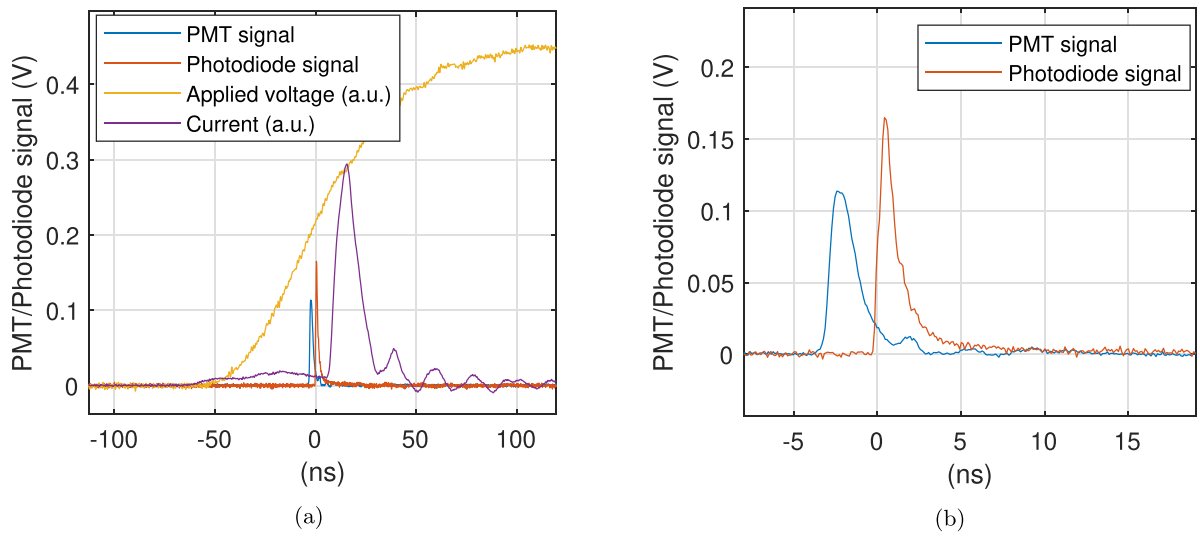

Figure 4. (a) Waveforms acquired in a single-shot measurement: PMT and photodiode signals in volts, and applied voltage and current, reported in arbitrary units. (b) Zoom in of the photodiode and PMT signals, corresponding to the 1st and 2nd harmonic signals.

This setup allows for real-time monitoring of the laser pulse intensity, which remains stable within a 1% margin. The laser energy used throughout the measurements is kept constant at ∼0.3 mJ. The voltage waveform is monitored by the internal electronics of the nanosecond-pulsed power supply using an integrated HV probe (Hivolt model PHV4002-3), which has a maximum voltage capacity of 40 kV and a bandwidth of 100 MHz. Simultaneously, the voltage at the HV electrode is measured using a HV probe (PMK PHV 4002-3, 1000:1 attenuation). The discharge current is measured using a Rogowski coil current monitor positioned on the ground electrode. All signals, including the voltage waveform, current, PD signal, and PMT output, are recorded using a Teledyne Lecroy oscilloscope (Lecroy HDO WavePro 404HD), which features a 4 GHz bandwidth and a sampling rate of 20 Gsample/s.

3.1. Single-shot measurements method

Unlike other EFISH measurements [34, 50], where the synchronization is dictated by the response time of the instruments, the present EFISH setup requires a different strategy. This limitation arises primarily from the intrinsic jitter introduced by the picosecond laser.

The master oscillator of the laser passively emits pulse trains at 87 MHz, resulting in an inherent timing jitter of approximately 11 ns upon external triggering. Although this issue can be mitigated by using the laser as the master trigger, the nanosecond-pulsed power supply lacks the functionality to receive external trigger signals, thereby preventing such a configuration. To overcome this, we adopt a single-shot acquisition method similar to that described in [51, 52], which allows us to counteract any jitter introduced by the trigger system.

Each single-shot measurement captures a snapshot of the electric field over a time window of approximately 28 ps, which corresponds to the duration of the laser pulse and defines the temporal resolution of the measurement. The timing of each measurement, instead, is determined during post-processing by measuring the delay between the laser pulse and the applied voltage. This delay is evaluated at the full width at half maximum (FWHM) of the PD signal and the voltage waveform, as shown in figure 4(a). The positive discharge, however, exhibits a temporal jitter of approximately 1 ns relative to the HV pulse, as previously reported in [34]. This jitter introduces a timing uncertainty in the EFISH measurements of about 1 ns relative to the positive plasma discharge. Since the triggering system of the nanosecond-pulsed power supply has a minimum time-step of 50 ns, we employ a pulse delay generator (Eksma SY4000-OEM) to achieve finer time-steps down to 100 ps. Compared to nanosecond EFISH measurements, the duration of the picosecond laser pulse is significantly shorter (∼28 ps) than the response time of both the PMT and the PD. As a result, the signals recorded by these detectors lack temporal resolution regarding the evolution of the electric field during the laser pulse. Due to this significant mismatch between the event duration and the response time of the detectors, if the electric field is assumed to be constant throughout the duration of the laser pulse, the electric field can be obtained from the EFISH signal produced by a single shot by integrating the PMT and PD signals, as described below:

$$E_{\text{ext}} = A\frac{\sqrt{\int I^{(2\omega)}(t)\mathrm{d}t}}{\int I^{(\omega)}(t)\,\mathrm{d}t} = A\cdot I_{\text{EFISH}}, \tag{1}$$

where E_{ext} is the measured electric field, A is a calibration constant whose dimensions are $\mathrm{V}^{3/2}\mathrm{s}^{1/2}\mathrm{m}^{-1}$, and $I^{(2\omega)}(t)$ and $I^{(\omega)}(t)$ are, respectively, the second harmonic at 532 nm and the first harmonic at 1064 nm, captured by the PMT and PD, as shown in figure 4(b) for a single-shot acquisition. For brevity, the square root of the time-integrated second harmonic signal normalized by the time-integrated fundamental intensity will

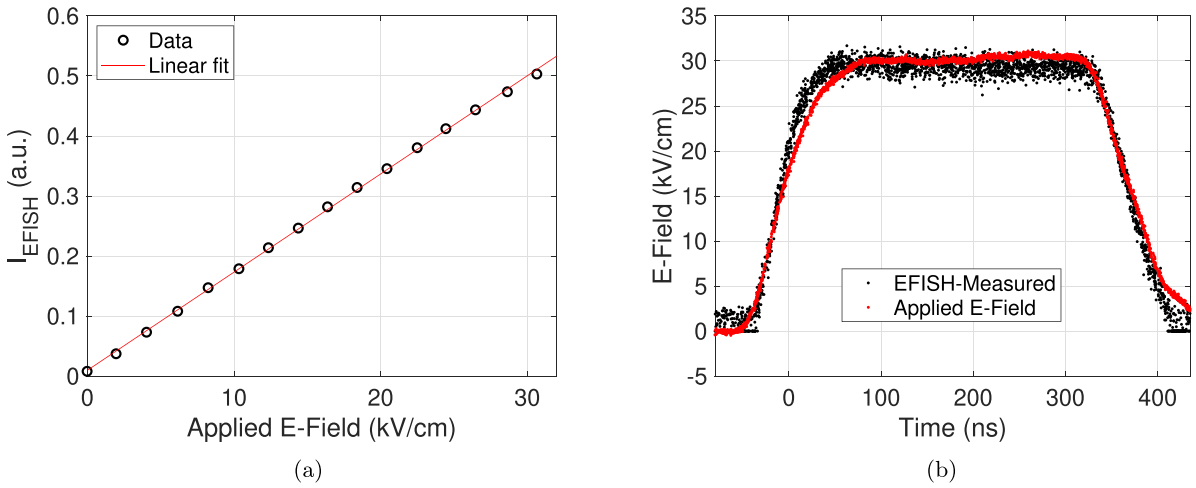

Figure 5. (a) EFISH signal in arbitrary units at increasing applied electric field in the inter-electrode gap of the VDBD. The measurements are taken at a fixed position in time at the flat top of the nanosecond pulse waveform where the electric field is constant, nominally at 200 ns (see (b)). (b) EFISH signal evolution over the duration of the nanosecond voltage pulse at 8 kV, expressed in kV cm^{-1} obtained from equations (1) and (2) within the inter-electrode gap of the VDBD.

hereafter be referred to as the EFISH signal I_{EFISH}. The conditions for performing EFISH measurements using a strongly focused laser, as highlighted in [53], are carefully considered. Firstly, the length of the VDBD electrodes $L = 2\,\mathrm{cm}$, which corresponds to the length of the plasma along the laser beam, is shorter than the coherence length in air, $L_{\mathrm{coh}} \simeq 6.28\,\mathrm{cm}$ [53]. Additionally, considering the symmetry of the parallel plate geometry of the VDBD, it is reasonable to assume that the electric field remains constant along the laser beam direction. This assumption holds under the condition that the plasma is diffused rather than filamentary, as already shown in [34]. Finally, second harmonic generation is gas-dependent, however, despite the presence of plasma-generated species, air remains the primary component of the gas mixture. The concentrations of these reactive species are expected to be on the order of parts per million (ppm), thus not significantly altering the overall gas composition and not influencing the EFISH measurements.

3.2. EFISH calibration

The calibration process is performed by applying a Laplacian electric field to the electrodes. The EFISH signal is acquired at the flat top of the nanosecond pulse waveform, where the electric field is constant, at increasing applied voltages below the plasma breakdown voltage. Since there is no plasma ignition, the electric field in the inter-electrode gap can be computed according to the following equation:

$$E_{\mathrm{app}}(t) = \frac{U_{\mathrm{app}}(t)}{d^*}, \tag{2}$$

where $U_{\mathrm{app}}(t)$ represents the applied voltage, and d^* is the effective gap distance, which accounts for the voltage drop due to the dielectric surfaces. Specifically, $d^* = d + 2l/\varepsilon_r$, where d equals 1.75 mm is the inter-electrode gap, $l = 0.66$ mm is the thickness of each dielectric layer, and $\varepsilon_r = 9.8$ is the relative dielectric constant of the alumina layer.

Subsequently, a calibration constant is obtained by performing a linear fit of the EFISH data against the electric field applied to the gap, as shown in figure 5(a). This analysis provides a calibration constant of approximately $A \simeq 60.5$. To evaluate the accuracy of this calibration, the temporal evolution of the EFISH signal during the nanosecond pulse waveform at a voltage below the plasma breakdown voltage, specifically at 8 kV, has been measured. The resulting data were calibrated using the constant A obtained from the linear fit and then compared to the applied electric field. In figure 5(b), the calibrated EFISH data, presented without any averaging or binning, for each individual shot, totaling approximately 3000 measurements, is plotted alongside the applied electric field. Notably, the EFISH measurements closely align with the applied electric field, confirming the reliability of the calibration constant and demonstrating the temporal accuracy of the EFISH data.

4. LIF experimental setup

The LIF measurements of NO and OH were conducted using a Nd:YAG pumped optical parametric oscillator laser (OPOTEK Opolette 355 LD) equipped with second and third harmonic generation, delivering a pulse duration of approximately ~ 7 ns.

The tuning of the wavelength can be achieved almost continuously in the 210–2400 nm range, with pulse energies extending up to 500 μJ at 225 nm and a maximum repetition rate of 20 Hz. The laser linewidth at the UV wavelength used for NO and OH is approximately 0.15 nm. The optical setup employed for the LIF measurements is illustrated in figure 6. The output from the OPO laser system is directed through a Pellin–Broca prism to select the desired wavelength. The

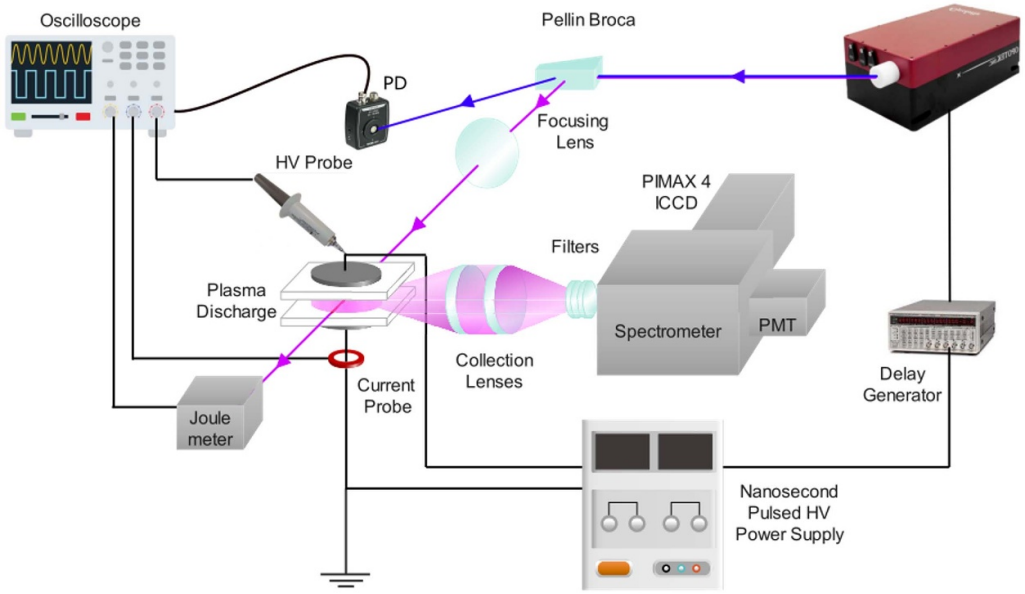

Figure 6. Schematic of the experimental setup used for the NO and OH LIF measurements.

third harmonic beam is then focused using a 30 cm UV-grade plano-convex lens to the plasma discharge region. The second harmonic instead is used to trigger the acquisition through a PD. The laser energy is monitored on a shot-by-shot basis after the beam passes through the discharge region using a Joulemeter (Gentec, ED-100A). This setup enables compensation of the LIF signal for laser energy fluctuations, ensuring measurement accuracy. Due to transmission losses through the optical components, the maximum laser energy entering the discharge zone is reduced by approximately 50%. The laser beam is oriented perpendicular to both the discharge axis and the optical axis of the LIF collection system. The optical detection is performed by collecting the plasma-induced fluorescence using two 30 cm focal length UV-grade quartz lenses. These lenses image the discharge gap (1:1 magnification) onto the entrance slit of a monochromator. The light is spectrally resolved by a 30 cm spectrometer (Acton Spectra Pro 2300), equipped with a multiple-grating turret with 300/600/1200 grooves mm^{-1}, blazed at 300 nm. In the current experiment, we used the 1200 groove mm^{-1} grating. The entrance and exit slits dimension defines the imaged collection area and can reach a maximum dimension of $3 \times 5\ mm^2$. In the current work, both slits horizontal dimension was fixed at 0.5 mm, that is the spatial horizontal resolution, and corresponds to a spectral window of approximately 1.5 nm. To avoid PMT signal saturation, intensity calibrated neutral density filters (Melles and Griot) were used whenever needed. The light is then acquired using a Hamamatsu PMT (model R928, spectral response 185–900 nm, pulse rise time 2.2 ns). The discharge voltage-charge and voltage-current characteristics were recorded using a Keysight InfiniiVision MSOX6004A with a bandwidth of 1 GHz and a sampling rate of up to 20 Gsamples/s. To measure the applied voltage, a Tektronix P6015A high voltage probe with a ratio of 1000:1 at 1 MΩ, a bandwidth of 25 MHz, and a rise time of 4.7 ns was employed. The current was measured using a Magnelab CT-c1.0 Rogowski coil with a rise time of 0.7 ns attached to the ground cable.

4.1. Nitric oxide (NO) LIF detection

The detection of NO by laser induced fluorescence has been performed by exciting the (0,0) band of $NO_\gamma(A^2\Sigma_u^+, X^2\Pi_r)$ system and detecting the emission from the excited level to the $\nu = 2{,}3$ of the ground electronic state at 247/260 nm. The laser has been tuned close to $\lambda_{NO} = 226.187$ nm centered around the $Q_{21}+Q_1$ band head. Due to the UV laser linewidth large enough to overlap several J lines of various sub-band of J manifold originating from a low and high rotational state, the resulting absorption remains nearly independent of temperature [54]. To filter out the laser scattered light we placed a 244 nm long-pass filter (Semrock LP02-244RS-25) and a 257/12 nm band-pass filter (Semrock FF01-257/12-25).

4.2. OH LIF detection

To detect the OH via LIF we used the excitation-detection scheme described in [55] which utilizes the dipole-allowed $OH(A^2\Sigma, \nu = 1)$ transition:

$$OH\left(X^2\Pi, v = 0\right) + h\nu_L \rightarrow OH\left(A^2\Sigma, v = 1\right),$$

$$OH\left(A^2\Sigma, v = 0, 1\right) \rightarrow OH\left(X^2\Pi, v = 0, 1\right) + h\nu_F.$$

The subscripts L and F refer to the laser (excitation photon) and fluorescence (detection photon), respectively. In this study, the laser excitation wavelength was set to $\lambda_{OH} = 282.05$ nm which nearly coincides with $Q_{11}(J = 1.5)$ rotational line of the (1,0) band at 282.07 nm. After pumping the rotational levels of the $OH(A^2\Sigma, \nu = 1)$ electronic state, the excitation energy is quickly redistributed due to fast rotational

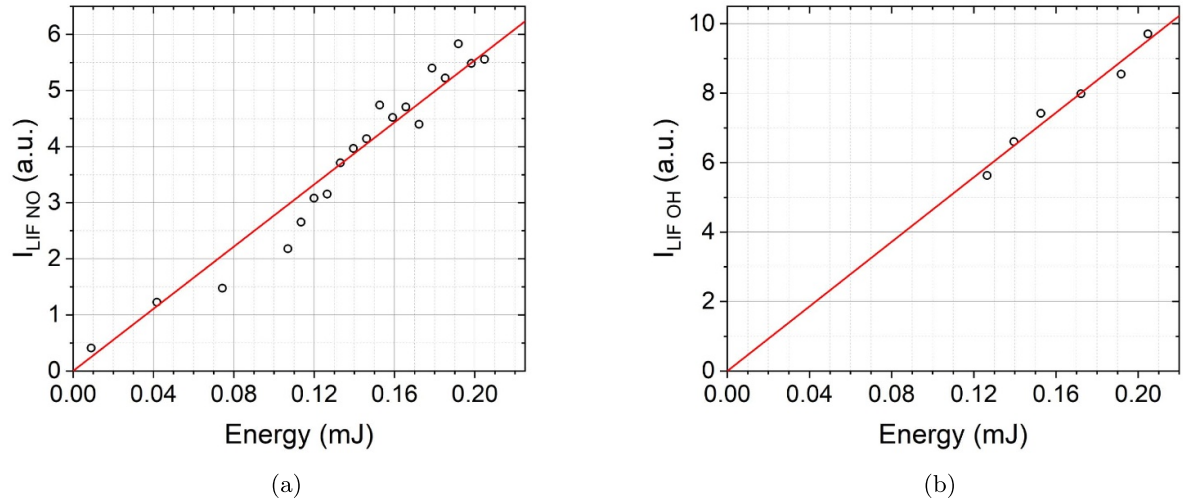

Figure 7. (a) Nitric oxide LIF saturation curve with respect to laser beam energy (data points in black and fit in red). (b) Hydroxil radical LIF saturation curve with respect to laser beam energy (data points in black and fit in red).

relaxation processes and, partly due to vibrational relaxation. Consequently, at atmospheric pressure, the observed fluorescence spectrum is usually characterized by a Boltzmann rotational distribution and emission originating from both $OH(A^2\Sigma, \nu = 0)$ and $OH(A^2\Sigma, \nu = 1)$ vibronic states. The fluorescence occurring in the 305–320 nm spectral region due to emission of (0,0) and (1,1) bands of the $OH(A^2\Sigma \rightarrow X^2\Pi)$ system, was detected by using an Hamamatsu R2949 photomultiplier and monochromator.

4.3. LIF linearity and calibration

The OH and NO LIF saturation curves in figure 7 indicate that, in the energy range considered, the system operates in a linear regime. At laser energies between 0.07 and 0.013 mJ, the apparent rate is slightly lower than that expected for a linear regime. This effect can be attributed to the non-uniform spatial profile of the laser beam and the spectral overlap between the laser line and the absorption lines. In the explored laser energy range, a linear response can be assumed as a good approximation to account for possible energy fluctuations (see figure 7). Therefore, laser fluctuations can be corrected by normalizing the fluorescence signal to the laser energy.

In both cases, NO and OH LIF, the laser energy is set at approximately $100\,\mu J\,pulse^{-1}$, corresponding to an energy density of $7.3 \times 10^3\,W\,cm^{-2}$. This setting represents an optimal compromise between spatial resolution and signal-to-noise ratio. The absolute calibration of the NO concentration in ppm is performed by acquiring the LIF signal while the reactor was saturated with a flow of 1 slm of gas mixtures of known NO concentration. The mixtures were obtained by blending pure air with a varying flow of an N_2/NO (Nippon Gases, certified gas mixture, 116 ± 7 ppm of NO in nitrogen) with a valid certificate. Syntethic Air (Nippon Gases, 5.0) was used to further dilute the gas flow to 1 slm in order to take into account the quenching phenomena occurring as the actual discharge is taking place (i.e. presence of both N_2 and, more prominently, O_2 in air).

5. Experimental results

5.1. EFISH measurements

The EFISH measurements were performed at three distinct vertical positions within the inter-electrode gap of the VDBD, as depicted in figure 8.

Thanks to the enhanced spatial filtering achieved by the pinhole adjustment and the use of a motorized vertical translation stage, we managed to achieve a beam width of approximately 270 μm at the edge of the dielectric plate. This value is measured using the motorized vertical stage and the PD, by monitoring the laser energy transmitted through the inter-electrode gap as the VDBD is moved vertically in fine steps. The laser beam width is calculated as the vertical distance over which the transmitted energy decreases from its maximum value to zero, corresponding to the beam being fully blocked by the VDBD structure.

The beam width at the focal point is instead calculated by using the Gaussian beam propagation equation to be $\omega_0 \leqslant 151\,\mu$m, assuming $M^2 \leqslant 2.5$ as specified by the laser manufacturer. This setup represents a substantial improvement compared to a previous work [34]. The three positions investigated were in the center of the VDBD gap, referred to as Center, and near the HV and grounded electrodes, denoted as HV and Ground, respectively. The voltage of the nanosecond pulse delivered to the VDBD was set at 11.6 kV. Figure 9 shows the EFISH measurements at the three laser positions, presented together for comparison. To improve data visualization, the single-shot measurements are binned in 1 ns intervals. However, the binning process averages individual shots within each bin, causing the loss of features that appear only in a few shots. To preserve the full information, the single-shot measurements, not binned, are shown separately in the close-ups of

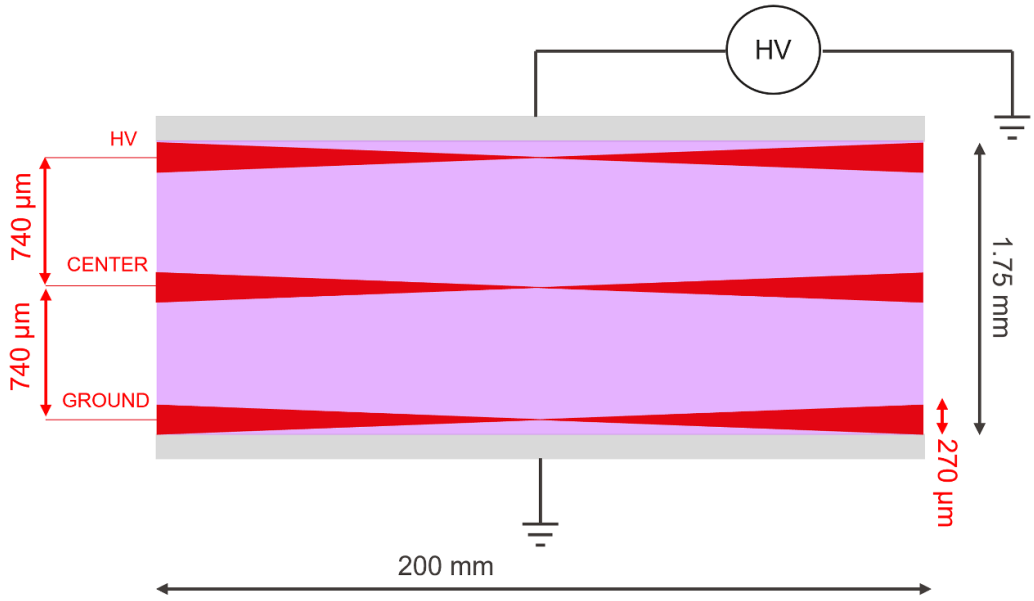

Figure 8. Position of the laser beam passing in the inter-electrode gap of the VDBD. The scheme shows the three distinct positions used for the EFISH measurements: Center, HV and Ground. The diagram also highlights that the beam width at the edge of the VDBD electrode measures approximately 270 μm.

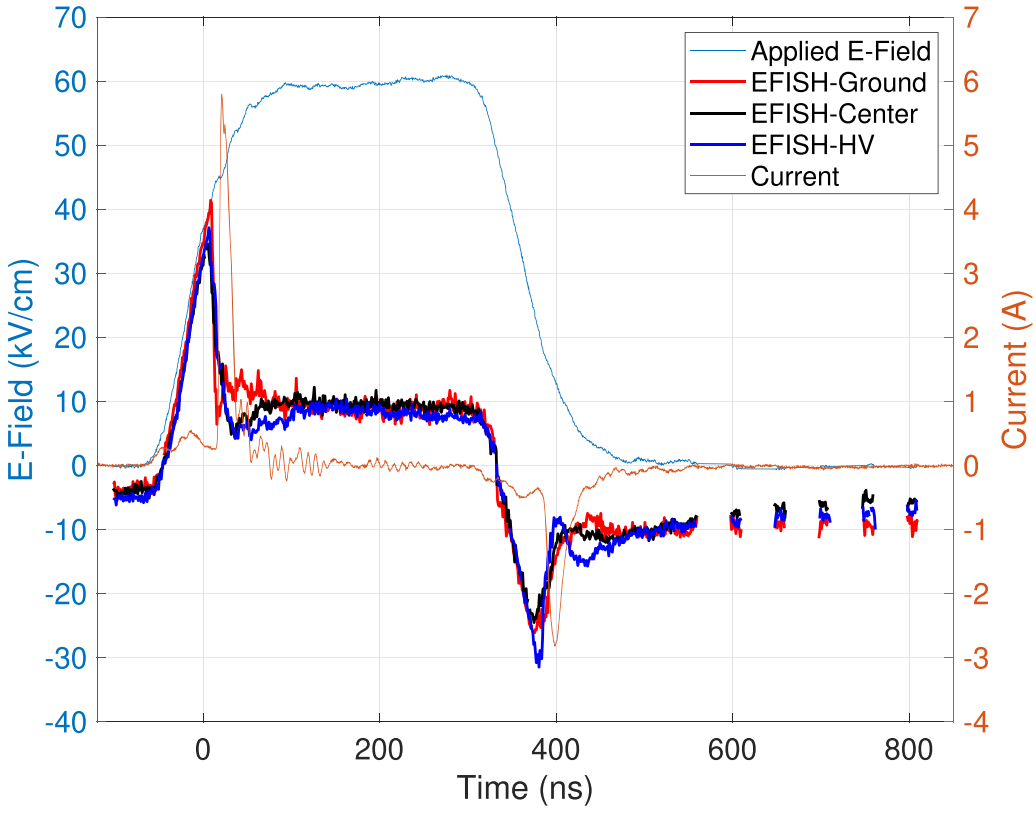

Figure 9. Calibrated and binned over 1 ns intervals EFISH measurements at the three different positions, namely Ground, Center and HV, within the inter-electrode gap of the VDBD. The applied electric field and the current are also reported.

the two plasma discharges, in figure 10. This approach reveals distinct features that were not detected in previous studies and would have been lost by binning or averaging.

As shown in figure 9, the EFISH signal is inverted at two specific discontinuity points, approximately −40 ns and 340 ns. This inversion is necessary when the electric field transitions between negative and positive values, in accordance with the direction of the current spikes. Since the PMT signal remains positive regardless of whether the vertically polarized second harmonic points upward or downward, the EFISH data

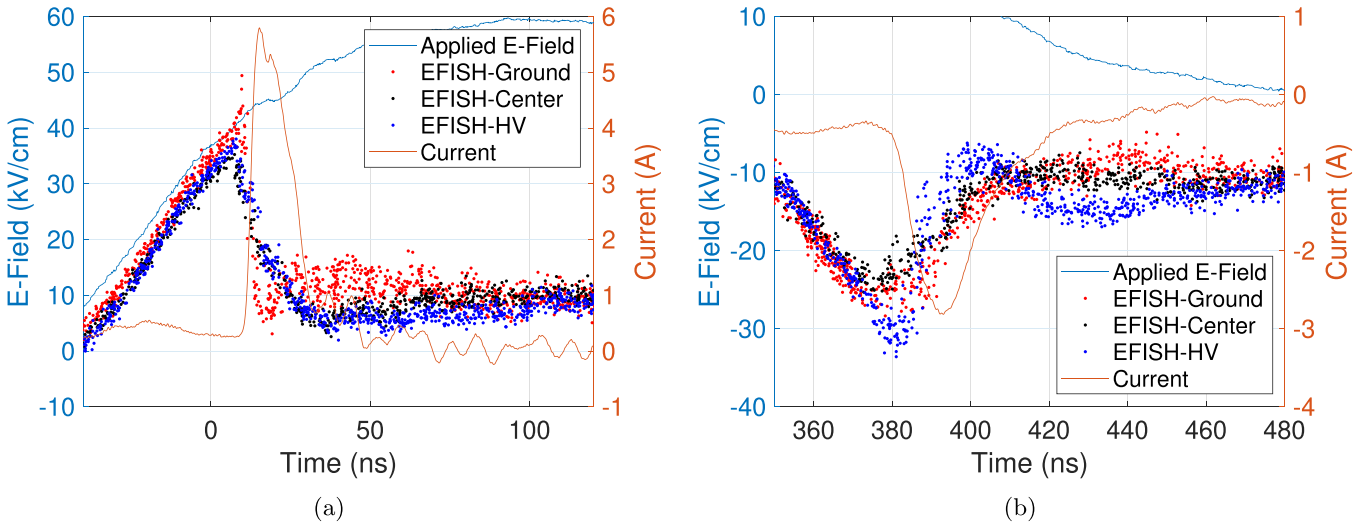

Figure 10. Close-ups of the single-shot EFISH measurements (not binned) in proximity of the positive (a) and negative (b) plasma discharges.

must be inverted to negative values before the rising edge and after the falling edge of the voltage pulse. Notably, the electric field is non-zero before and after the voltage waveform, indicating the presence of a residual field likely caused by charge accumulation on the surfaces of the VDBD dielectrics. As expected, two distinct electric field peaks, followed by rapid drops, are observed in correspondence of the two plasma discharges, whereas the electric field maintains an approximately constant value of 10 kV cm^{-1} between the two plasma discharges, rather than decaying to zero. These findings are in agreement with previous observations reported in [34].

The results, however, indicate significant differences between the Ground position and the other two positions near the positive plasma discharge. In contrast, during the negative plasma discharge, the HV position exhibits differences compared to the other two positions. A detailed examination of the three single-shot datasets near the positive plasma discharge, shown in figure 10(a), reveals that the electric field reaches higher values before breakdown at the Ground position than at the other positions. Furthermore, a pronounced surge in the electric field, up to approximately 50 kV cm^{-1}, is observed in a few single-shot measurements precisely at the moment of the first plasma breakdown. This behavior is consistent with the 'overshoot' phenomenon reported in other configurations [52, 56], although it had not been experimentally observed in this setup until now. This phenomenon, captured only by a few measurements, lasts for just a few nanoseconds during the ionization wave propagation. Assuming the ionization wave traverses the entire VDBD inter-electrode gap, this 'overshoot' should theoretically appear at all three measurement positions. However, despite acquiring a large dataset of up to 3800 single-shot measurements per position, this overshoot is absent at the Center and HV positions. Following the plasma breakdown, the electric field decreases and then recovers to a stable value more rapidly at the Ground position compared to the HV and Center positions. This difference is significant considering the electric field drop occurs in roughly 5 ns, consistent with earlier kinetic models developed for this setup [34]. This pattern, observed during the positive plasma discharge at the Ground position is similarly reflected during the negative plasma discharge at the HV position, shown in detail in figure 10(b). Just before the negative plasma discharge, the HV position presents a higher electric field compared to the other positions. Moreover, the reduction and recovery of the electric field after the negative plasma discharge are faster at the HV position. These results demonstrate notable differences, not only between the center of the plasma discharge volume and the region closer to the dielectric surface, but also between the ground and HV electrodes, caused by the dynamics of the charged particles. Additionally, since the EFISH measurements were taken at a distance of 270 μm from the dielectric surfaces on both ground and HV sides, it is likely that even greater differences in the evolution of the electric field could be observed closer to the dielectric interface.

5.2. NO and OH LIF measurements

As shown in figure 11(a), a baseline NO concentration of approximately 0.7 ppm is maintained between HV pulses. The NO concentration starts to increase as the voltage increases and when the plasma discharge is ignited. Notably, during the plasma discharges it was still possible to follow the NO LIF signal at $\lambda = 247$ nm by subtracting the background emission. After the plasma discharges, the concentration of NO increases over time as chemistry progresses, reaching its maximum value of approximately 1.8 ppm after approximately 100 μs. After a few hundreds of microseconds, the NO concentration starts to decrease, returning to its base value before the next voltage pulse is initiated.

The OH radical, on the other hand, is mainly formed during the plasma discharges as a result of the dissociation of water vapor in humid air. This behavior is evident from the sharp increase in signal intensity immediately following the voltage

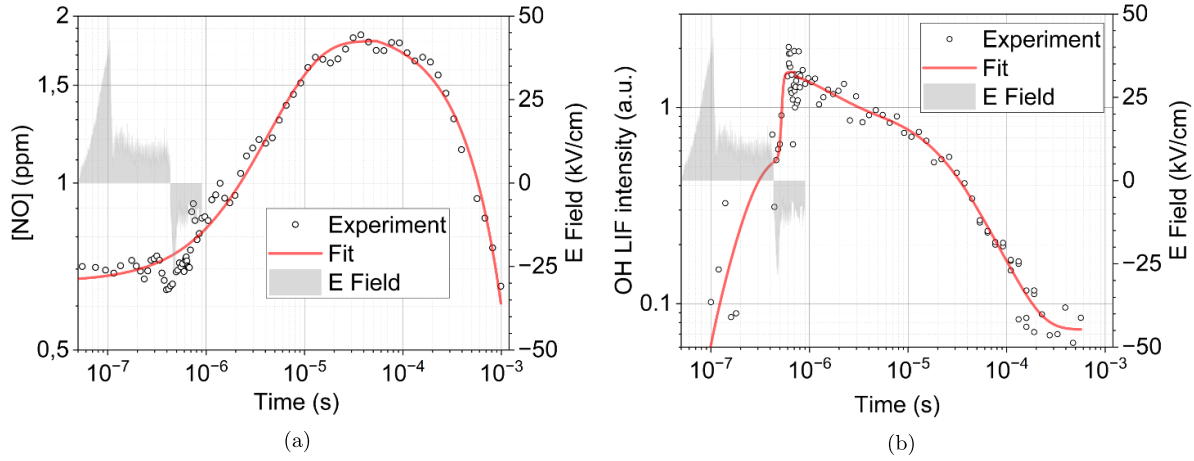

Figure 11. (a) NO concentration in ppm (data points in black and fit in red) in between HV pulses at 11.6 kV, and 1 kHz repetition frequency. (b) OH relative concentration (data points in black and fit in red) in between HV pulses at 11.6 kV, and 1 kHz repetition frequency. Grey areas represent the E-field measured by EFISH. The time axis and the NO concentration and OH LIF intensity axis. are represented on a logarithmic scale.

pulse, as shown in figure 11(b). A steady decline in OH concentration is observed during the afterglow until the start of the next voltage pulse. Interestingly, the decay rate appears to slow over time, eventually exhibiting a small shoulder in the decay profile. The fitting curves shown in figure 11 do not accurately represent the data points, but are intended to merely highlight graphically the growth and decay trends of the LIF signals of the detected species.

6. Computational model

The homogeneous behavior of the studied plasma discharge was modeled using a volume-averaged (0D) kinetic approach. This method is commonly chosen for its computational efficiency, especially when simulating complex chemical systems. The time evolution of the volume-averaged species number densities was computed using the MERLINO code, developed at the University of Bologna. The implemented species conservation equation is given by:

$$\frac{\mathrm{d}n_s}{\mathrm{d}t} = \sum_j \left[\left(a^R_{sj} - a^L_{sj}\right) k_j \prod_l n_l \right] + R_{\mathrm{in},s} - R_{\mathrm{out},s}, \qquad (3)$$

where a^R_{sj} and a^L_{sj} are the right-hand side and left-hand side stoichiometric coefficients of species s in the reaction j, k_j is the rate coefficient of reaction jth, n_l are the number densities of the species involved in reaction jth. $R_{\mathrm{in},s}$ and $R_{\mathrm{out},s}$ represent the number density rate of change for the species s due to the in-flow and out-flow, respectively.

$R_{\mathrm{in},s}$ can be expressed as [57, 58]:

$$R_{\mathrm{in},s} = c\frac{Q_s P_{\mathrm{atm}}}{V k_B T_{\mathrm{in}}}, \qquad (4)$$

where Q_s is the partial volume flow rate (in sccm) introduced in the plasma domain, c is a conversion factor, P_{atm} is the atmospheric pressure, V is the plasma volume, k_B is the Boltzmann constant and $T_{\mathrm{in}} = 300\,\mathrm{K}$ is the temperature of the in-flow. Note that $Q_s \neq 0$ only for N_2, O_2 and H_2O and, given a total flux $Q = \sum_s Q_s = 1000\,\mathrm{sccm}$, the partial fluxes can be obtained as $Q_{N2} = 0.78Q$, $Q_{O2} = 0.19Q$ and $Q_{H2O} = 0.03Q$. Similarly, R_{out}, s, that is needed to ensure the mass conservation during the simulation (i.e. that the mass flowing in the volume corresponds to the one exiting it) can be expressed as:

$$R_{\mathrm{out},s} = cQ\frac{P_{\mathrm{atm}} T_g}{V P T_{\mathrm{in}}} n_s, \qquad (5)$$

where T_g is the gas temperature, P is the gas pressure. Note that $\frac{P_{\mathrm{atm}}}{P} \sim 1$ and that in this study we consider $T_g = T_{\mathrm{in}} = 300\,\mathrm{K}$.

The model incorporates a reaction set consisting of nearly 5000 processes, involving the species listed in table 1. The considered gas mixture, representing saturated humid air at atmospheric pressure with ~100% of relative humidity (RH), is composed by 78% of N_2, 19% of O_2 and 3% of H_2O. The reaction set, described in detail in [41], includes electron impact reactions [37, 59] (ionization, attachment, excitation), vibrational kinetics of N_2 [42, 43, 60] and collision between neutrals [37, 44]. Rate coefficients of electron impact reactions have been obtained by solving the electron Boltzmann equation (EBE) for different values of the reduced electric field using the Lisbon KInetics Boltzmann (LoKI-B) solver [61, 62], that adopts the two-terms approximation. The correspondent cross sections have been obtained from the online database LXCat [63–65].

To account for the effects of background ionization, a constant source term equal to $5 \times 10^{18}\mathrm{m}^{-3}\mathrm{s}^{-1}$ is added to electrons and O_2^+ ions. The corresponding electron number density with zero applied field, is $n_{e,0} = 10^{12}\mathrm{m}^{-3}$. While n_{e0} values in previous literature span 6 orders of magnitude (from $10^8\mathrm{m}^{-3}$ to $10^{14}\mathrm{m}^{-3}$) [66, 67]), we chose the reported value based on previous works on pulsed DBDs in similar conditions [34].

Table 1. Species considered in the simulations. Each vibrationally-excited level is treated like a single species. O_2(Sum) represents the sum of the states $O_2(A^3\Sigma_u^+)$, $O_2(C^3\Delta_u)$ and $O_2(c^1\Sigma_u^-)$.

N_2(X, $0 \leqslant v \leqslant 59$), $N_2(A^3\Sigma_u^+)$, $N_2(B^3\Pi_g)$, $N_2(C^3\Pi_u)$, $N_2(a'\Sigma_u^-)$, $N_2(w^1\Delta_u)$, $N_2(a^1\Pi_g)$, N_2^+, $N_2{}^+(B^2\Sigma_u^+)$
$N(^4S)$, $N(^2D)$, $N(^2P)$, N^+, $N_4{}^+$, $N_3{}^+$
O_2, $O_2(a^1\Delta_g)$, $O_2(b^1\Sigma_g^+)$, O_2(Sum), $O_2{}^+$, O_2^-
$O(^3P)$, $O(^1D)$, O^+, O^-, O_3, O_3(exc), $O_3{}^-$, O_4^-, $O_4{}^+$
NO, $NO(A^2\Sigma^+)$, $NO(B^2\Pi)$, NO^+, NO^-, NO_2, $NO_2{}^+$, $NO_2{}^-$, NO_2(A)
NO_3, $NO_3{}^-$, N_2O(X), N_2O^+, N_2O^-, N_2O_3, N_2O_4, N_2O_5
H_2O, H_2O^+, H_3O^+, H, H^+, H^-, OH, OH^+, OH^-, H_2, $H_2{}^+$, $H_3{}^+$, HO_2, H_2O_2
HNO, HNO_2, HNO_3, e

7. Simulation results

In this section, the described computational model is used to simulate the plasma produced in the VDBD described in the previous paragraphs. At each simulation time step, the reduced electric field value is enforced according to the one measured by EFISH during the period of the plasma discharge. The experimentally measured reduced field values were first processed using the `envelope` algorithm of MATLAB's Signal Processing Toolbox. The algorithm was used with the 'peak' option activated, together with a spline interpolation over local maxima separated by at least 5 samples. Since the EFISH measurements did not cover the entire period of the voltage waveform, we assumed an exponentially decaying electric field beyond the last measured point. The time constant of this decay was chosen so that the E/N value at the end of the period matched the measured value at the start of the following cycle. The simulations are then performed by repeating the reduced field waveform until the species number densities reach a periodic state (200 pulses in this work). We emphasize that the simulations in this work were performed using the electric field waveform measured near the ground electrode of the real device, marked as EFISH-Ground in figure 9. Among the three experimentally measured profiles, this waveform exhibited the highest peak value and provided the best agreement between simulated and measured chemical species concentration. We postulate that the electric field measured in the vicinity of the ground electrode acts as the main driver for the discharge kinetics. Indeed, due to the lower peak values reached by the other two electric fields, the number densities predicted by the corresponding simulations are several order of magnitudes lower than those measured experimentally. We also note that the employed electric field waveform is comparable to the one that was self-consistently derived in [34], using a one-dimensional time-dependent model. Therefore, through higher-resolution time-resolved electric field measurements and the adoption of a more advanced kinetic model, this work provides supporting evidence for the electric field behavior predicted numerically in [34].

The following sections focus on the simulated behavior of neutral and charged species over a time-period of the applied voltage, after the species have reached a periodic steady state.

7.1. Neutrals

7.1.1. Nitric oxide. The simulation results and the experimental measurements are compared over one period of the applied voltage in figure 12. The blue line represents the NO behavior predicted by the model. The concentration increases slightly during the discharge phase, then the species undergoes a step-like increase at the end of the voltage pulse at 4×10^{-7} s, corresponding to the negative plasma discharge. Note that the experimental data do not report the step-like behavior mentioned above. This discrepancy is probably due to some missing processes between electrons and NO molecules in the kinetic scheme, that can play an important role when the reduced field is higher (i.e. during the rise and fall of the external voltage). Subsequently, the concentration increases further during the post-discharge phase, reaching a maximum value of about 1 ppm at 5×10^{-5}. The model closely matches the experimental data within 1×10^{-6}, during the plasma discharge phase, and right before the following voltage pulse, at 1×10^{-3}. A slight discrepancy ($\sim$0.8 ppm) can be observed in the post-discharge phase, between 1×10^{-6} and 1×10^{-4}, which might be explained by the fact that photoionization is not addressed by the model. The red line in figure 12, shows the outcome obtained by adding a simplified photoionization mechanism, which will be discussed further below.

To gain more insight into the physical behavior of NO, the main creation and destruction mechanisms governing the NO number density are reported in figure 13.

It is shown that NO is mainly created through the following reaction:

$$O_2 + N(^2D) \rightarrow NO + O(^1D). \tag{6}$$

However, it plays an important role exclusively when the value of the reduced electric field applied to the plasma discharge is high enough to produce $N(^2D)$ atoms through the reaction:

$$e + N_2 \rightarrow e + N(^4S) + N(^2D). \tag{7}$$

Consequently, NO is efficiently formed only during the plasma discharge phase ($\sim$20 μs after the plasma discharge

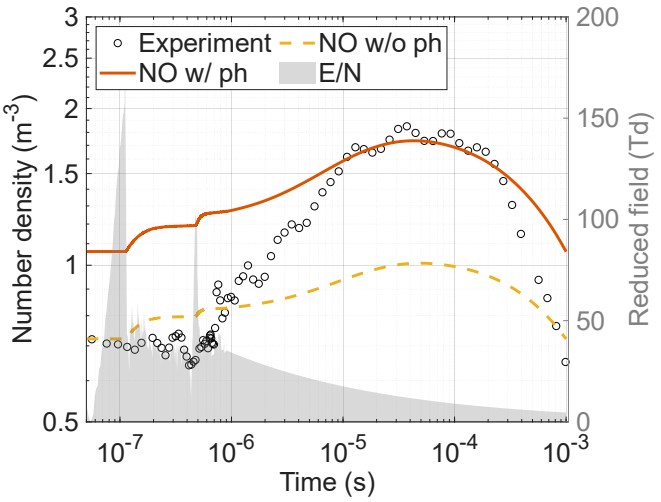

Figure 12. Comparison between measured and simulated NO number density during one period of the applied voltage, with and without the photoionization mechanism; E/N is the reduced electric field used in the simulation, inferred from EFISH measurements.

ignition). The importance of N(^{2}D) in pulsed plasma discharges has also been shown in [68].

Referring to figure 12, NO starts to decrease after $\sim 3 \times 10^{-5}$ s due to two mechanisms:

$$\mathrm{NO} + \mathrm{OH} + \mathrm{M} \rightarrow \mathrm{HNO_2} + \mathrm{M}, \tag{8}$$

$$\mathrm{NO} + \mathrm{O3} \rightarrow \mathrm{NO_2} + \mathrm{O_2}, \tag{9}$$

where M represents N_2, O_2 and H_2O. Reactions (8) and (9) are characterized by different behaviors related to the different lifetimes of O_3 and OH molecules. In fact, the reaction rate of process (8) is dominant for the first half of the considered time span, but then starts to decrease due to the relatively low lifetime of OH. Conversely, during the second half, the main reaction rate is the one of the process (9), that remains nearly constant for all the considered voltage source waveform time period due to the long lifetime of ozone molecules. The temporal evolution of the reaction rates is reported in figure 13(b). To conclude this analysis, the contribution of other NO formation mechanisms, including for instance vibrational kinetics, have been considered. In different kinds of discharges, ranging from low pressure DC (stationary or pulsed) glow discharges [42, 69] to atmospheric pressure sinusoidal DBD [38, 39] one of the most important creation channel for NO is constituted by the Zeldovich mechanism:

$$\mathrm{N_2}\,(v > 12) + \mathrm{O}(^3\mathrm{P}) \rightarrow \mathrm{NO} + \mathrm{N}(^4\mathrm{S}). \tag{10}$$

However, in this study, the population of the vibrationally excited nitrogen molecules is quite low, as reported in figure 14, and therefore does not contribute to NO formation under the condition studied in this work. This is expected, since a key factor for the population of the vibrational distribution function (VDF) is constituted by the electron number density. It is well known, in fact, that a higher electron number density corresponds to a more populated VDF [70], due to the effect of the e–V collisions:

$$\mathrm{e} + \mathrm{N_2}\,(v) \leftrightarrow \mathrm{e} + \mathrm{N_2}\,(v+1)\,. \tag{11}$$

In the present case study, during one period of the voltage source, the electron number density is significantly high only for a very short time span and, as a consequence, e–V collisions are not effectively activated. Moreover, N_2 intermediate vibrational levels are mainly created by V–V collisions:

$$\mathrm{N_2}\,(v) + \mathrm{N_2}\,(w) \leftrightarrow \mathrm{N_2}\,(v-1) + \mathrm{N_2}\,(w+1)\,, \tag{12}$$

and their number density increases more slowly compared to the first levels. Consequently, the convective flux, which depletes vibrational populations from the considered volume, prevents the effective buildup of intermediate levels.

Other mechanisms that were also considered involve high electronically excited states of N_2 reported in equation:

$$\mathrm{N_2}\,(\cdot) + \mathrm{O}(^3\mathrm{P}) \rightarrow \mathrm{NO} + \mathrm{N}(^4\mathrm{S}), \tag{13}$$

with $N_2(\cdot) = N_2(\mathrm{B}^3\Pi_g)$, $\mathrm{N_2}(\mathrm{C}^3\Pi_u)$, $\mathrm{N_2}(\mathrm{a}'\Sigma_u^-)$, $\mathrm{N_2}(\mathrm{w}^1\Delta_u)$, $\mathrm{N_2}(\mathrm{a}^1\Pi_g)$. These reactions, proven to be important for the kinetics of a nanosecond-pulsed discharge in air [71], have nearly no effect in our simulation. This is due to the difference between the value of the reduced electric field in [71] (with a peak value of ∼350 Td) and the ones measured in this work (with a peak value of ∼200 Td).

As mentioned before, the simulated NO dynamics differ from the measured one in correspondence to the peak value of the NO, see figure 12 at $\sim 5 \times 10^{-5}$ s. This could be related to the lack of photoionization mechanisms in the adopted reactions set. Several studies in the literature [66, 72, 73] highlight the significance of photoionization in air, particularly in pulsed DBD discharges. Specifically, highly energetic photons can be produced through the spontaneous de-excitation of electronically-excited nitrogen molecules $\mathrm{N_2}(b^1\Pi_v)$ and $\mathrm{N_2}(b^1\Sigma_v)$ [73], which have energies of 12.771 eV and 13.371 eV, respectively. The reactions for spontaneous de-excitation are shown in reactions (14) and (15).

$$\mathrm{N_2}\left(\mathrm{b}^1\Pi_v\right) \rightarrow \mathrm{N_2} + \nu, \tag{14}$$

$$\mathrm{N_2}\left(\mathrm{b}^1\Sigma_v\right) \rightarrow \mathrm{N_2} + \nu. \tag{15}$$

These photons have energies higher than the ionization energy of O_2 molecules (i.e. 12.07 eV), and so they can cause ionization, producing an electron and an oxygen ion, as represented in reaction (16).

$$\nu + \mathrm{O_2} \rightarrow \mathrm{O_2}^+ + \mathrm{e}. \tag{16}$$

While important for detailed photo-ionization models, the excited states $\mathrm{N_2}(b^1\Pi_v)$ and $\mathrm{N_2}(b^1\Sigma_v)$ are not included in the current kinetic model, as they generally exhibit low steady-state densities and a limited impact on the global chemistry of the discharge [74] due to their high energy

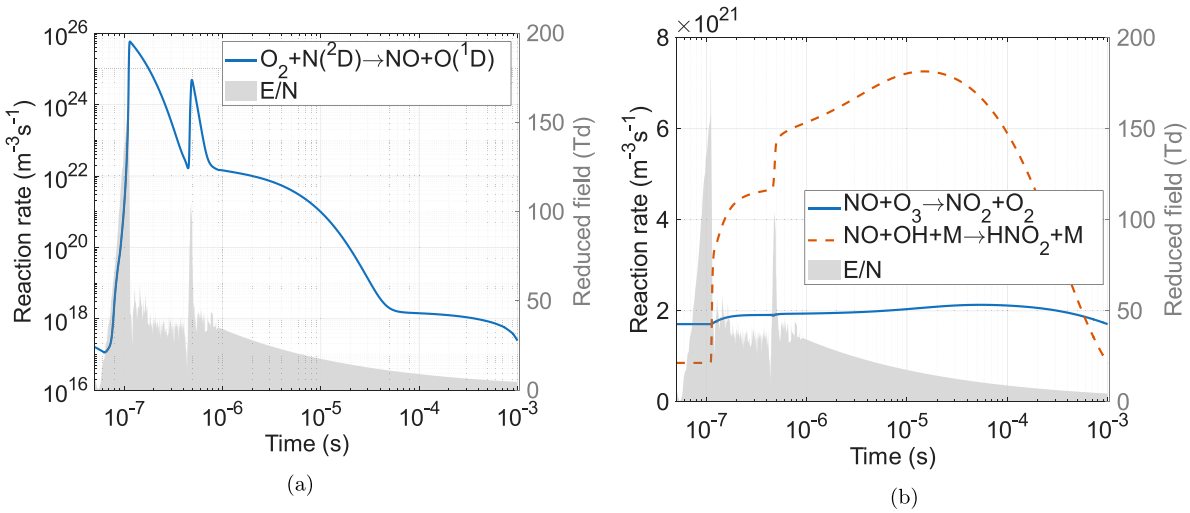

Figure 13. (a) Reaction rates for the main formation (a) and loss (b) mechanisms of NO. M represents N_2, O_2 and H_2O; E/N is the reduced electric field used in the simulation, inferred from EFISH measurements.

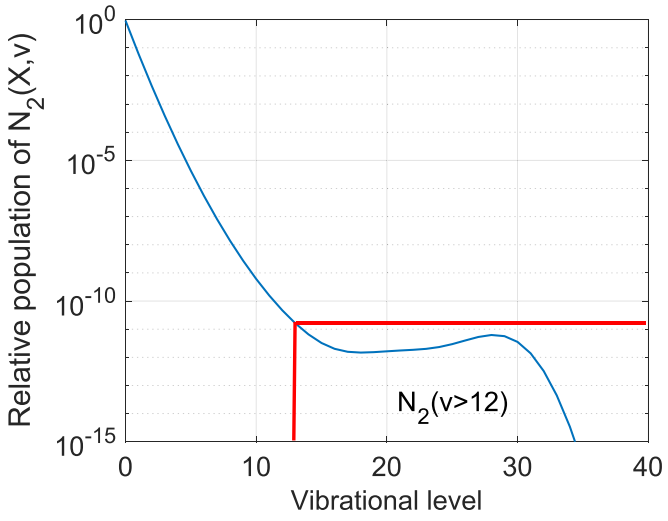

Figure 14. Vibrational distribution function of N_2 molecules immediately before the ignition of a voltage pulse. The part of the VDF contributing to NO formation is highlighted in red.

thresholds. Furthermore, photo-ionization is inherently a spatially non-uniform process,,driven by photon transport and local absorption, which poses significant challenges for implementation in 0D (global) plasma models. To address these challenges, a simplified approach is adopted to account for photoionization effects. It should be noted that the purpose of this approach is not to precisely simulate photoionization, but rather to provide an explanation for the discrepancies between measured and simulated peak values of NO during the post-discharge phase.

In this context, we assume that the $N_2(C^3\Pi_u)$ state can spontaneously de-excite to form the $N_2(B^3\Pi_g)$ state, releasing a photon with sufficient energy to ionize an oxygen molecule (∼12.08 eV [74]). The energy of the $N_2(C^3\Pi_u)$ state (approximately 11 eV [65, 74]) is indeed reasonably close to the one of the $N_2(b^1\Pi_v)$ state (∼12.5 eV [74]). Additionally, we assume that the released photon immediately ionizes the oxygen molecule. The resulting reaction added to the model is as follows:

$$N_2\left(C^3\Pi_u\right) \rightarrow N_2\left(B^3\Pi_g\right) + {O_2}^+ + e, \qquad (17)$$

with a reaction rate that corresponds to the one of the spontaneous de-excitation of $N_2(C^3\Pi_u)$, i.e. $k_{17} = 2.74 \times 10^7\,s^{-1}$ [37]. We acknowledge that this simplification may overestimate the number of electrons produced by photoionization processes. Moreover, this simplified mechanism increases the number of available electrons throughout the whole simulation, leading to the ∼0.3 ppm discrepancy with the NO measurements before and after the maximum at $\sim 5 \times 10^{-5}$ s in figure 12. However, as mentioned earlier, the goal of this approach is to investigate whether photoionization or other sources of electrons not included in the original reaction set (such as electron inception from alumina dielectric layers due to photon or ion bombardment) could improve the agreement between simulated and measured NO number densities, as shown in figure 12.

7.1.2. Hydroxyl radical. The comparison between experimental measurements and simulation results for OH molecules, reported in figure 15, shows an overall good agreement. Nonetheless, some degree of discrepancy can be observed at around $\sim 10^{-6}$ s.

To gain more insight into the dynamics of OH, we focus on the main creation and loss mechanisms of OH during one nanosecond pulse and the subsequent afterglow before the next pulse. The reactions that contribute to OH formation are numerous and related to the kinetics of different chemical species characterized by different lifetimes. The largest contribution to OH production comes from reactions combining

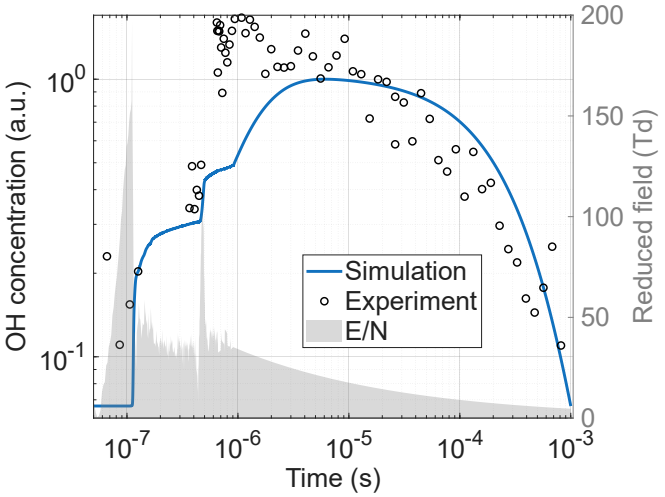

Figure 15. Comparison between LIF measurements and simulations of OH number density; E/N is the reduced electric field used in the simulation, inferred from EFISH measurements.

atomic oxygen and nitrogen excited states $O(^1D)$ and $N(^2D)$ with water:

$$O(^1D) + H_2O \rightarrow OH + OH, \tag{18}$$

$$N(^2D) + H_2O \rightarrow OH + NH. \tag{19}$$

Conversely, electronically-excited states of N_2

$$N_2(A) + H_2O \rightarrow OH + H + N_2, \tag{20}$$

do not seem to play a significant role in the OH formation (see e.g. [75] for a discussion on the impact of electronically-excited states on OH dynamics for an Argon plasma jet). The observation that $N_2(A)$ does not affect OH kinetics suggests that higher excited states are also unlikely to influence this species, given their typically shorter lifetimes. Other mechanisms that play a less prominent but still relevant role in OH creation are the electron impact reaction

$$e + H_2O \rightarrow e + OH + H, \tag{21}$$

and the ionic charge-exchange reaction

$$OH^- + O_3 \rightarrow O_3^- + OH, \tag{22}$$

favored by the ozone-rich environment created within the discharge gap.

Regarding OH loss mechanisms, these are related to both short- and long-lived species. After the discharge ignition, the main reaction contributing to OH depletion involves oxygen atoms:

$$O(^3P) + OH \rightarrow H + O_2. \tag{23}$$

However, since the atomic-oxygen lifetime is relatively short, this mechanism loses importance for longer times, when OH depletion becomes dominated by other species (i.e. O_3, NO_2, HO_2), through reactions:

$$OH + HO_2 \rightarrow O_2 + H_2O, \tag{24}$$

$$OH + NO_2 + M \rightarrow HNO_3 + M, \tag{25}$$

$$O_3 + OH \rightarrow HO_2 + O_2, \tag{26}$$

$$OH + HNO_2 \rightarrow NO_2 + H_2O. \tag{27}$$

The observed discrepancy between the experimental and numerical prediction of the OH peak value suggests that the model may not fully capture the underlying physical processes. Although an insufficient density of free electrons might seem a plausible explanation, the simulated OH peak remains unaffected by the inclusion or exclusion of photoionization (reaction (17)). This observation implies that the discrepancy is not primarily due to the absolute rate of electron production, but rather to the dynamics governing how electrons are generated and made available through the various kinetic mechanisms considered in the model.

A plausible explanation could involve secondary electron emission from the dielectric barrier, induced by ion bombardment, which is not accounted for in the current simulations. While secondary emission is surely present during both positive and negative plasma discharges, we expect it to be mostly relevant during the negative discharge, because the concentration of ions is much larger at that stage compared to the positive discharge. Furthermore, the use of the quasi-steady-state approximation in solving the Boltzmann equation to determine the electron energy distribution function (EEDF) may introduce errors in estimating the rate coefficients for impact ionization processes [76]. This approximation might fail to fully capture the fast timescales associated with the electric fields involved, potentially leading to an incomplete representation of the electron dynamics. Experimentally, it was observed that the E/N deduced from the ratio of the nitrogen SPS and FNS bands did not reproduce the electric field measured by EFISH [34]. This observation led to the hypothesis of a non-local contribution to the EEDF, potentially from a beam of fast electrons accelerated in the cathode fall, similar to what is observed in the negative glow of a low-pressure Townsend discharge. However, such a hypothesis cannot be adequately explained by a global modeling approach. Instead, it might be addressed through detailed modeling techniques, such as particle-in-cell Monte Carlo collision simulations, which can account for non-local effects.

7.2. Charged species

As reported in figure 9, the reduced electric field presents a plateau after the plasma breakdown. Previous one-dimensional drift-diffusion modeling results [34] suggested that this plateau can be caused by long-lived ionic negative species, whose number densities in the discharge gap remain significant for the entire duration between two consecutive pulses. Clearly, the negative space charge in the gap must be compensated by a corresponding amount of positive charged

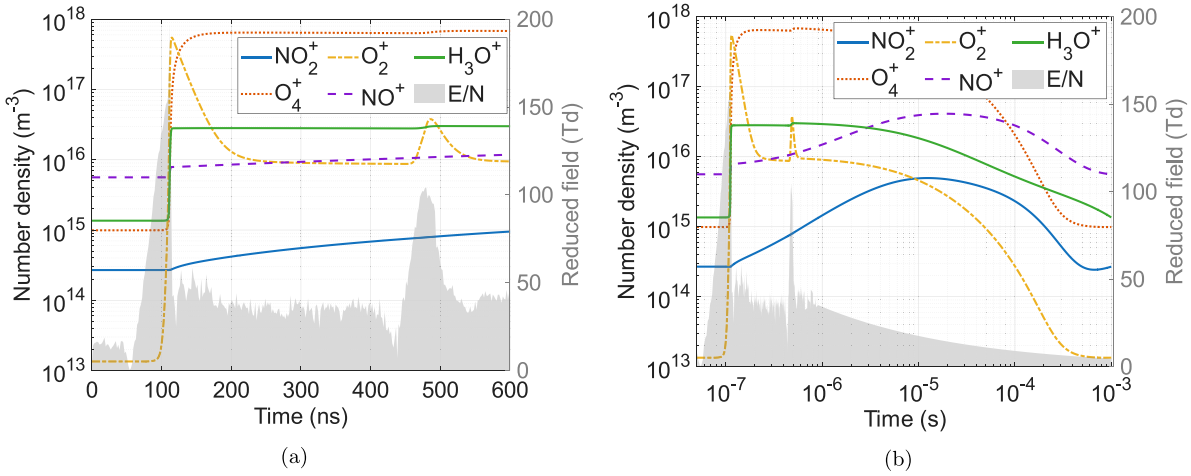

Figure 16. Simulation of selected positive ions over 600 ns scale (a) and over 1 ms (b); E/N is the reduced electric field used in the simulation, inferred from EFISH measurements.

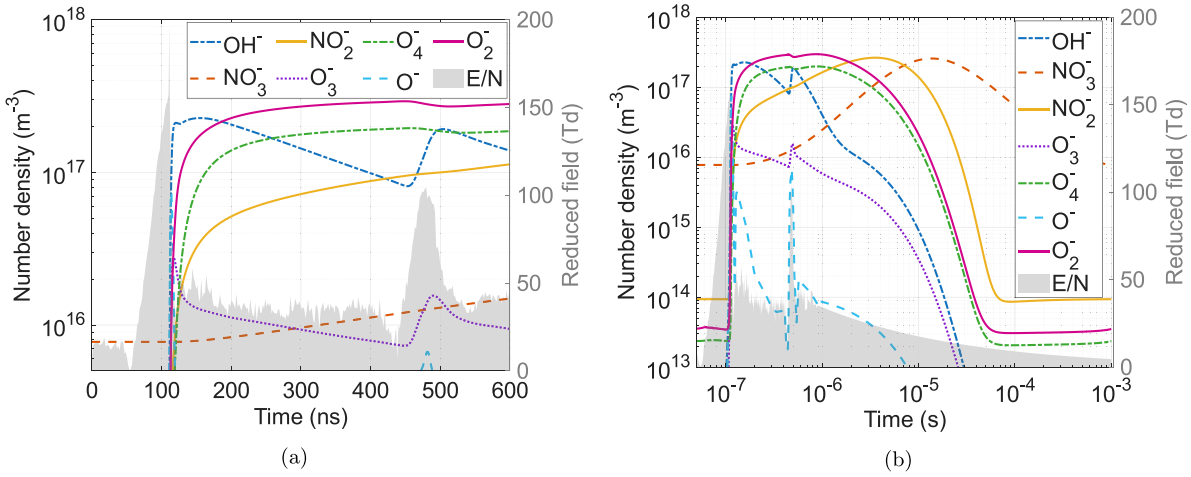

Figure 17. Simulation of selected negative ions over 600 ns scale (a) and over 1 ms (b); E/N is the reduced electric field used in the simulation, inferred from EFISH measurements.

particles, probably in the form of surface charge. The combination of the surface charge and the negative charge in the gap leads to the observed stable electric field. Since a more detailed kinetic model is employed in this work, an additional analysis of the charged species is carried out here to identify the main anions and cations generated by the plasma discharge. The evolution of positive and negative charged species is shown in figures 16 and 17, respectively, during the 200th period of the voltage source waveform, where the densities have reached a periodic steady state.

Figure 16 shows that several cations contribute to the total positive charge concentration. Immediately after the plasma discharge ignition, $O_2{}^+$ is initially the most abundant species, produced via electron impact ionization, but it is quickly surpassed by $O_4{}^+$ formed by the three-body recombination reaction:

$$O_2{}^+ + O_2 + M \rightarrow O_4{}^+ + M. \tag{28}$$

After ∼160 ns, $O_4{}^+$ reaches a concentration that is two orders of magnitude higher than those of $O_2{}^+$, H_3O^+, and NO^+. Over longer time scales, the situation changes significantly. As shown in figure 16(b), the concentration of $O_2{}^+$ decreases rapidly until it reaches a number density of $10^{13}\mathrm{m}^{-3}$, while $O_4{}^+$ drops by nearly three orders of magnitude due to the charge recombination reaction with $NO_3{}^-$:

$$O_4{}^+ + NO_3{}^- \rightarrow NO_3 + O_2 + O_2. \tag{29}$$

Before the next voltage pulse is ignited, its number density is similar to that of H_3O^+ (i.e. around $2 \times 10^{15}\mathrm{m}^{-3}$). The most abundant positive ion species between two pulses is NO^+ whose kinetics is controlled by the charge exchange processes with neutral species and, of course, NO molecules.

Regarding the negative ions, figure 17(a) shows that immediately following the ignition of the plasma discharge, OH^-, O_2^-, and O_4^- are the predominant species, with a number density close to $10^{17}\mathrm{m}^{-3}$. As mentioned earlier in this section, these negative species are responsible for maintaining a stable electric field value of approximately $10\,\mathrm{kV\,cm}^{-1}$ after the positive plasma discharge. The electrons generated during the plasma breakdown are rapidly consumed to form negative

ions. Due to the significantly greater inertia of these ions compared to electrons, the electric field does not collapse to zero but instead remains stable [34]. On the other hand, for a longer time scale reported in figure 17(b), NO_3^- is by far the most abundant anion, with a number density that is two orders of magnitude larger than that of O_2^-, O_4^- and NO_2^-. Conversely, OH^- is completely depleted after $\sim$500 μs from the plasma discharge ignition and its concentration changes by more than seven orders of magnitude between two consecutive voltage pulses. NO_3^- is created mainly through charge exchange reactions between NO_2^- (whose number density changes by nearly 4 orders of magnitude between two consecutive discharges) and long-lived species (i.e. O_3 and HNO_3) that are reported below:

$$NO_2^- + O_3 \rightarrow NO_3^- + O_2, \tag{30}$$

$$NO_2^- + HNO_3 \rightarrow NO_3^- + HNO_2. \tag{31}$$

Note that, due to the scarcely populated N_2 VDF in these conditions, O_3 reaches a high concentration of $\sim$0.1% of relative population, making the conversion of NO_2^- in NO_3^- very effective. Moreover, the long lifetime of both ozone and HNO_3, makes the creation of NO_2^- ions difficult during the afterglow phases, promoting instead the formation of NO_3^- which consequently is the most abundant ionic species during the time interval between two different pulses. The long lifetime of NO_3^- is confirmed by different published studies [37, 77].

8. Conclusion

In this study, we present a comprehensive analysis of the electric field and the dynamics of key radical species within a VDBD in saturated humid air at atmospheric pressure. This analysis combines EFISH generation and LIF techniques. The electric field measurements serve as input for a 0D kinetic model, which we validated using LIF measurements of the concentration of NO and OH. Our findings offer significant insights into the spatial and temporal evolution of the electric field and reactive species during both the plasma discharge and the post-discharge phase.

The EFISH measurements confirmed key findings from [34], including a persistent electric field of approximately 10 kV cm^{-1} following the positive plasma discharge and a residual field between HV pulses, probably caused by charge accumulation on the dielectric surfaces. By employing a spatial filter optical setup and a picosecond laser, we achieved improved spatial (270 μm) and temporal (28 ps) resolution compared to the previous study. This enhanced resolution allowed us to detect previously unobserved features and revealed significant differences in the electric field dynamics at three distinct locations across the discharge gap: Ground, Center, and HV. Specifically, the Ground position exhibited a higher electric field prior to the positive plasma discharge, with an observed 'overshoot' phenomenon reaching up to 50 kV cm^{-1} in some single-shot measurements. This overshoot, although not consistently observed at all positions, aligns with the phenomena reported in other experimental configurations and kinetic models [34, 52, 56]. Furthermore, the electric field reduction and subsequent stabilization right after plasma breakdown occurred more rapidly at the Ground position compared to the HV and Center positions, a pattern that was mirrored during the negative plasma discharge at the HV position. These observations highlight distinct temporal dynamics across the three regions, as consistently shown by the EFISH data. Additionally, since EFISH measurements were taken at a distance of 270 μm from the dielectric surfaces on both ground and HV sides, it is likely that even greater differences in the evolution of the electric field could be observed closer to the dielectric surface. Further investigation is needed to elucidate the mechanisms underlying these spatial variations and to explore their implications for plasma-based technologies. To gain a more complete picture of plasma behavior, LIF measurements were employed to assess the evolution of key reactive species, such as NO and OH. NO concentration increased sharply during the discharge and peaked shortly afterward before gradually declining, reflecting ongoing post-discharge chemistry. OH radicals, largely generated via water dissociation, exhibited a rapid spike followed by a steady decrease during the afterglow phase. These findings improve our understanding of radical generation and decay in VDBDs, offering a basis for optimizing discharge conditions in applied settings.

Incorporating EFISH measured electric field data into our 0D kinetic model enabled a robust simulation framework. It should be noted that other techniques that are commonly used to estimate the reduced field in a volumetric DBD reactor in 0D simulations (e.g. using an equivalent circuit model) cannot take into account the effect of the space charge. Consequently, the value of the reduced electric field in the discharge gap could be greatly underestimated, with detrimental effects on the simulation results. Knowledge of the temporal evolution of the electric field enables the execution of detailed and reliable kinetic simulations. This approach was validated by the strong agreement between the simulated results and the experimental LIF measurements for both NO and OH radicals. Specifically, the simulated NO dynamics showed a minimal difference of just 0.7 ppm compared to the measured data, underscoring the precision of the model. This discrepancy can be partly attributed to the omission of the photoionization process, which may play an important role in this setup. When photoionization is included, the experimental and computational results show good agreement in between HV pulses. Furthermore, accounting for secondary electron emission mechanisms could further enhance the consistency between the simulations and experimental observations. For OH dynamics, the simulation results were largely consistent with the experimental data, although some discrepancies were observed around 10^{-6} seconds. These differences suggest that, while the model effectively captures the primary formation and decay mechanisms, additional processes, such

as secondary electron emissions from dielectric barriers, may play a role that is not fully represented in the current model. Furthermore, the model results showed that the possible negative ions responsible for the non-zero electric field after the plasma breakdown are OH^-, O_2^- and O_4^-.

It is important to note that, while the 0D model results refer to the spatial average number densities within the discharge gap, the reduced field used by the model is the one measured in the vicinity of the ground electrode. This location exhibited the highest field among the three measured positions and is therefore assumed to be the primary driver of the discharge kinetics. However, this assumption introduces a potential limitation in the current approach. To address this, future work should consider the implementation of 1D or 2D kinetic models, which could improve the reliability of the simulations and provide deeper insight into the spatial dependence of the electric field dynamics. Such models may help clarify why the higher electric field observed at plasma breakdown, likely associated with the ionization wave, is confined to the region near the grounded electrode and not present across the entire gap.

Overall, the integration of EFISH measurements into our simulation not only validated the experimental findings but also provided deeper insights into the plasma discharge processes. This study highlights the importance of using precise electric field measurements to refine kinetic models, paving the way for future research to further enhance our understanding of LTP dynamics and its applications.

Data availability statement

The data cannot be made publicly available upon publication because no suitable repository exists for hosting data in this field of study. The data that support the findings of this study are available upon reasonable request from the authors.

Acknowledgments

This Project was funded under the National Recovery and Resilience Plan (NRRP), Mission 4 Component 2 Investment 1.3 - Call for tender No. 1561 of 11.10.2022 of Ministero dell'Universitá e della Ricerca (MUR); funded by the European Union—NextGenerationEU, Award Number: Project code PE0000021, Concession Decree No. 1561 of 11.10.2022 adopted by Ministero dell'Universitá e della Ricerca (MUR), CUP J33C22002890007, Project title 'Network 4 Energy Sustainable Transition—NEST' ISTP activities were supported by Regione Puglia, Riparti—POC PUGLIA FESRT-FSE 2014/2020 and the Italian National Recovery and Resilience Plan (NRRP), funded by the European Union-NextGenerationEU (Mission 4, Component 2, Investment 3.1-Area ESFRI Energy-Call for tender No. 3264 of 28-12-2021 of Italian University and Research Ministry (MUR), Project ID IR0000007 'NEFERTARI-', MUR Concession Decree No. 243 del 04/08/2022, CUP B53C22003070006). The work was funded by the European Union under NextGenerationEU. PRIN 2022 Prot. n. 2022J5NBBN Project PLASMODD. IPFN activities were supported by the Portuguese FCT, under Projects UIDB/50010/2020 (https://doi.org/10.54499/UIDB/50010/2020), UIDP/50010/2020 (https://doi.org/10.54499/UIDP/50010/2020) and LA/P/0061/2020 (https://doi.org/10.54499/LA/P/0061/2020).

Author contributions

Lorenzo Ibba 0000-0003-1900-3618
Conceptualization (lead), Data curation (lead), Formal analysis (lead), Investigation (lead), Methodology (lead), Project administration (supporting), Software (equal), Supervision (supporting), Validation (equal), Visualization (lead), Writing – original draft (lead), Writing – review & editing (lead)

Giacomo Pierotti 0000-0003-1973-0612
Conceptualization (supporting), Data curation (lead), Formal analysis (lead), Investigation (equal), Methodology (equal), Software (lead), Validation (equal), Visualization (lead), Writing – original draft (equal), Writing – review & editing (equal)

Arturo Popoli 0000-0002-0990-8053
Conceptualization (equal), Data curation (equal), Formal analysis (equal), Investigation (equal), Methodology (equal), Project administration (supporting), Software (equal), Supervision (equal), Validation (equal), Visualization (supporting), Writing – original draft (lead), Writing – review & editing (lead)

Domenico Aceto 0000-0002-5748-8962
Data curation (equal), Formal analysis (equal), Investigation (equal), Methodology (supporting), Software (supporting), Visualization (equal), Writing – original draft (supporting), Writing – review & editing (supporting)

Carlos D Pintassilgo 0000-0003-1527-2976
Funding acquisition (equal), Methodology (supporting), Resources (supporting), Software (equal), Supervision (equal)

Andrea Cristofolini 0000-0001-5896-6615
Conceptualization (equal), Funding acquisition (lead), Methodology (supporting), Project administration (equal), Resources (equal), Supervision (equal), Validation (equal), Investigation (supporting), Writing – review & editing (supporting)

Paolo F Ambrico 0000-0002-2455-6949
Conceptualization (equal), Data curation (equal), Formal analysis (equal), Funding acquisition (equal), Investigation (equal), Methodology (equal), Resources (equal), Software (supporting), Supervision (equal), Validation (equal), Visualization (equal), Writing – original draft (supporting), Writing – review & editing (equal)

Ivo Furno 0000-0001-8348-1716
Conceptualization (lead), Funding acquisition (lead), Investigation (supporting), Methodology (equal), Project administration (lead), Resources (lead), Supervision (lead), Validation (supporting), Writing – review & editing (equal)

References

[1] Duarte P B S and Panariello B H D 2020 Comprehensive biomedical applications of low temperature plasmas *Arch. Biochem. Biophys.* **693** 108560

[2] Laroussi M *et al* 2022 Low-temperature plasma for biology, hygiene and medicine: perspective and roadmap *IEEE Trans. Radiat. Plasma Med. Sci.* **6** 127–57

[3] Ambrico P F, Šimek M, Morano M, Angelini R M D M, Minafra A, Trotti P, Ambrico M, Prukner V and Faretra F 2017 Reduction of microbial contamination and improvement of germination of sweet basil (ocimum basilicum l.) seeds via surface dielectric barrier discharge *J. Phys. D: Appl. Phys.* **50** 305401

[4] Ambrico P F, Šimek M, Ambrico M, Morano M, Prukner V, Minafra A, Allegretta I, Porfido C, Senesi G S and Terzano R 2019 On the air atmospheric pressure plasma treatment effect on the physiology, germination and seedlings of basil seeds *J. Phys. D: Appl. Phys.* **53** 104001

[5] Waskow A, Howling A and Furno I 2021 Mechanisms of plasma-seed treatments as a potential seed processing technology *Front. Phys.* **9** 617345

[6] Konchekov E M, Gusein-zade N, Burmistrov D E, Kolik L V, Dorokhov A S, Izmailov A Y, Shokri B and Gudkov S V 2023 Advancements in plasma agriculture: a review of recent studies *Int. J. Mol. Sci.* **24** 10

[7] Jiang H, Lin Q, Shi W, Yu X and Wang S 2022 Food preservation by cold plasma from dielectric barrier discharges in agri-food industries *Front. Nutrit.* **9** 11

[8] Birania S, Attkan A K, Kumar S, Kumar N and Singh V K 2022 Cold plasma in food processing and preservation: a review *J. Food Process Eng.* **45** 9

[9] Moldgy A, Nayak G, Aboubakr H A, Goyal S M and Bruggeman P J 2020 Inactivation of virus and bacteria using cold atmospheric pressure air plasmas and the role of reactive nitrogen species *J. Phys. D: Appl. Phys.* **53** 434004

[10] Woedtke T V, Schmidt A, Bekeschus S, Wende K and Weltmann K-D 2019 Plasma medicine: a field of applied redox biology *In Vivo* **33** 1011–26

[11] Fridman G, Peddinghaus M, Balasubramanian M, Ayan H, Fridman A, Gutsol A and Brooks A 2006 Blood coagulation and living tissue sterilization by floating-electrode dielectric barrier discharge in air *Plasma Chem. Plasma Process.* **26** 425–42

[12] Chen Z, Chen G, Obenchain R, Zhang R, Bai F, Fang T, Wang H, Lu Y, Wirz R E and Gu Z 2022 Cold atmospheric plasma delivery for biomedical applications *Mater. Today* **54** 153–88

[13] Laroussi M 2020 Cold plasma in medicine and healthcare: the new Frontier in low temperature plasma applications *Front. Phys.* **8** 74

[14] Min T, Xie X, Ren K, Sun T, Wang H, Dang C and Zhang H 2022 Therapeutic effects of cold atmospheric plasma on solid tumor *Front. Med.* **9** 884887

[15] Keidar M, Walk R, Shashurin A, Srinivasan P, Sandler A, Dasgupta S, Ravi R, Guerrero-Preston R and Trink B 2011 Cold plasma selectivity and the possibility of a paradigm shift in cancer therapy *Br. J. Cancer* **105** 1295–301

[16] Živanić M, Espona-Noguera A, Lin A and Canal C 2023 Current state of cold atmospheric plasma and cancer-immunity cycle: therapeutic relevance and overcoming clinical limitations using hydrogels *Adv. Sci.* **10** 3

[17] Sakudo A, Yagyu Y and Onodera T 2019 Disinfection and sterilization using plasma technology: fundamentals and future perspectives for biological applications *Int. J. Mol. Sci.* **20** 10

[18] Ibba L, Agus R, Avino F, Furno I and Ambrico P 2023 In-situ FTIR and laser induced fluorescence RONS characterization of atmospheric pressure nanosecond-pulsed surface DBD plasma for indirect treatments of E.Coli *Plasma Chem. Plasma Process.* **44** 785–805

[19] Ziuzina D, Patil S, Cullen P J, Keener K M and Bourke P 2013 Atmospheric cold plasma inactivation of escherichia coli in liquid media inside a sealed package *J. Appl. Microbiol.* **114** 778–87

[20] Ziuzina D, Boehm D, Patil S, Cullen P J and Bourke P 2015 Cold plasma inactivation of bacterial biofilms and reduction of quorum sensing regulated virulence factors *PLoS One* **10** 1–21

[21] Das S, Gajula V P, Mohapatra S, Singh G and Kar S 2022 Role of cold atmospheric plasma in microbial inactivation and the factors affecting its efficacy *Health Sci. Rev.* **4** 100037

[22] Beyrer M, Smeu I, Martinet D, Howling A, Pina-Pérez M C and Ellert C 2020 Cold atmospheric plasma inactivation of microbial spores compared on reference surfaces and powder particles *Food Bioprocess Technol.* **13** 827–37

[23] Kostov K G, Rocha V, Koga-Ito C Y, Matos B M, Algatti M A, Honda R Y, Kayama M E and Mota R P 2010 Bacterial sterilization by a dielectric barrier discharge (DBD) in air *Surf. Coat. Technol.* **204** 2954–9

[24] Leipold F, Schultz-Jensen N, Kusano Y, Bindslev H and Jacobsen T 2011 Decontamination of objects in a sealed container by means of atmospheric pressure plasmas *Food Control* **22** 1296–301

[25] Ambrico P F, Šimek M, Rotolo C, Morano M, Minafra A, Ambrico M, Pollastro S, Gerin D, Faretra F and Angelini R M D M 2020 Surface dielectric barrier discharge plasma: a suitable measure against fungal plant pathogens *Sci. Rep.* **10** 12

[26] Juswono U P, Santjojo D J D H, Kasa R A and Faisal M 2023 Bacterial sterilization using non-thermal plasma method surface dielectric barrier discharge (SBDB): effect of treatment duration on colony count, DNA, protease enzymes and cell morphology *Trends Sci.* **20**

[27] Tanino M, Xilu W, Takashima K, Katsura S and Mizuno A 2005 Sterilization using dielectric barrier discharge at atmospheric pressure *Conf. Record - IAS Annual Meeting (IEEE Industry Applications Society)* vol 2 pp 784–8

[28] Seri P, Nici S, Cappelletti M, Scaltriti S G, Popoli A, Cristofolini A and Neretti G 2023 Validation of an indirect nonthermal plasma sterilization process for disposable medical devices packed in blisters and cartons *Plasma Process. Polym.* **20** e2300012

[29] Orr K, Tang Y, Simeni M S, van den Bekerom D and Adamovich I V 2020 Measurements of electric field in an atmospheric pressure helium plasma jet by the e-fish method *Plasma Sources Sci. Technol.* **29** 035019

[30] Dogariu A, Goldberg B M, O'Byrne S and Miles R B 2017 Species-independent femtosecond localized electric field measurement *Phys. Rev. Appl.* **7** 024024

[31] Huang B, Zhang C, Adamovich I, Akishev Y and Shao T 2020 Surface ionization wave propagation in the nanosecond pulsed surface dielectric barrier discharge: the influence of dielectric material and pulse repetition rate *Plasma Sources Sci. Technol.* **29** 044001

[32] Simeni M S, Baratte E, Zhang C, Frederickson K and Adamovich I V 2018 Electric field measurements in nanosecond pulse discharges in air over liquid water surface *Plasma Sources Sci. Technol.* **27** 015011
[33] Cui Y, Zhuang C and Zeng R 2019 Electric field measurements under DC corona discharges in ambient air by electric field induced second harmonic generation *Appl. Phys. Lett.* **115** 244101
[34] Ambrico P F, Aceto D, Ibba L, Yang X, Dilecce G, Ambrico M, Furno I and Adamovich I V 2023 Breakdown development in a nanosecond pulsed dielectric barrier discharge in humid air in plane-to-plane geometry *Plasma Sources Sci. Technol.* **32** 095008
[35] Bobkova E S, Smirnov S A, Zalipaeva Y V and Rybkin V V 2014 Modeling chemical composition for an atmospheric pressure dc discharge in air with water cathode by 0-d model *Plasma Chem. Plasma Process.* **34** 721–43
[36] Komuro A, Ono R and Oda T 2010 Kinetic model of vibrational relaxation in a humid-air pulsed corona discharge *Plasma Sources Sci. Technol.* **19** 055004
[37] Sakiyama Y, Graves D B, Chang H-W, Shimizu T and Morfill G E 2012 Plasma chemistry model of surface microdischarge in humid air and dynamics of reactive neutral species *J. Phys. D: Appl. Phys.* **45** 425201
[38] Shimizu T, Sakiyama Y, Graves D B, Zimmermann J L and Morfill G E 2012 The dynamics of ozone generation and mode transition in air surface micro-discharge plasma at atmospheric pressure *New J. Phys.* **14** 103028
[39] Pierotti G, Piferi C, Popoli A, Cavedon M, Cristofolini A, Martines E and Riccardi C 2023 A novel two-stage kinetic model for surface DBD simulations in air *Plasma Sources Sci. Technol.* **32** 064005
[40] Stefanovic I, Bibinov N, Deryugin A, Vinogradov I, Napartovich A and Wiesemann K 2001 Kinetics of ozone and nitric oxides in dielectric barrier discharges in O2/NOx and N2/O2/NOx mixtures *Plasma Sources Sci. Technol.* **10** 406
[41] Pierotti G, Popoli A, Pintassilgo C D and Cristofolini A 2024 Modeling study of chemical kinetics and vibrational excitation in a volumetric DBD in humid air at atmospheric pressure *Plasma Chem. Plasma Process.* **44** 1–20
[42] Guerra V, Caz A T-del, Pintassilgo C D and Alves L L 2019 Modelling N2–O2 plasmas: volume and surface kinetics *Plasma Sources Sci. Technol.* **28** 073001
[43] Alves L L, Marques L, Pintassilgo C D, Wattieaux G, Es-Sebbar E, Berndt J, Kovacević E, Carrasco N, Boufendi L and Cernogora G 2012 Capacitively coupled radio-frequency discharges in nitrogen at low pressures *Plasma Sources Sci. Technol.* **21** 045008
[44] Pintassilgo C D 2012 Plasma chemistry in repetitively pulsed discharges in air at low pressures *Plasma Sources Sci. Technol.* **21** 035020
[45] Unfer T and Boeuf J-P 2010 Modeling and comparison of sinusoidal and nanosecond pulsed surface dielectric barrier discharges for flow control *Plasma Phys. Control. Fusion* **52** 124019
[46] Popoli A, Ragazzi F, Pierotti G, Neretti G and Cristofolini A 2023 A Boltzmann electron drift diffusion model for atmospheric pressure non-thermal plasma simulations *Plasma* **6** 393–407
[47] Heirman P, Van Boxem W and Bogaerts A 2019 Reactivity and stability of plasma-generated oxygen and nitrogen species in buffered water solution: a computational study *Phys. Chem. Chem. Phys.* **21** 12881–94
[48] Colonna G, D'Ammando G and Pietanza L D 2016 The role of molecular vibration in nanosecond repetitively pulsed discharges and in DBDS in hydrogen plasmas *Plasma Sources Sci. Technol.* **25** 054001
[49] Ibba L 2023 Characterization of low-temperature plasmas generated by dielectric barrier discharges for bacterial inactivation *PhD Thesis* EPFL
[50] Adamovich I V, Butterworth T, Orriere T, Pai D Z, Lacoste D A and Cha M S 2020 Nanosecond second harmonic generation for electric field measurements with temporal resolution shorter than laser pulse duration *J. Phys. D: Appl. Phys.* **53** 145201
[51] Chng T L, Orel I S, Starikovskaia S M and Adamovich I V 2019 Electric field induced second harmonic (e-fish) generation for characterization of fast ionization wave discharges at moderate and low pressures *Plasma Sources Sci. Technol.* **28** 045004
[52] Orr K, Yang X, Gulko I and Adamovich I V 2020 Formation and propagation of ionization waves during ns pulse breakdown in plane-to-plane geometry *Plasma Sources Sci. Technol.* **29** 12
[53] Chng T L, Starikovskaia S M and Schanne-Klein M-C 2020 Electric field measurements in plasmas: how focusing strongly distorts the e-fish signal *Plasma Sources Sci. Technol.* **29** 125002
[54] Dilecce D B S *et al* 2007 $N_2(A^3\Sigma_u^+)$ density measurement in a dielectric barrier discharge in N_2 and N_2 with small O_2 admixtures *Plasma Source Sci. Technol.* **16** 511
[55] Dilecce G, Ambrico P, Simek M and Benedictis S D 2011 Lif diagnostics of hydroxyl radical in atmospheric pressure he-H_2O dielectric barrier discharges *Chem. Phys.* **398** 142–7
[56] Chng T L, Brisset A, Jeanney P, Starikovskaia S M, Adamovich I V and Tardiveau P 2019 Electric field evolution in a diffuse ionization wave nanosecond pulse discharge in atmospheric pressure air *Plasma Sources Sci. Technol.* **28** 09LT02
[57] Kemaneci E, Mitschker F, Benedikt J, Eremin D, Awakowicz P and Brinkmann R P 2019 A numerical analysis of a microwave induced coaxial surface wave discharge fed with a mixture of oxygen and hexamethyldisiloxane for the purpose of deposition *Plasma Sources Sci. Technol.* **28** 115003
[58] He Y *et al* 2021 Zero-dimensional and pseudo-one-dimensional models of atmospheric-pressure plasma jets in binary and ternary mixtures of oxygen and nitrogen with helium background *Plasma Sources Sci. Technol.* **30** 105017
[59] Budde M, Dias T C, Vialetto L, Pinhao N, Guerra V and Silva T 2022 Electron-neutral collision cross sections for H_2O: I. complete and consistent set *J. Phys. D: Appl. Phys.* **55** 445205
[60] Bourdon A and Vervisch P 2000 Analytical models for electron-vibration coupling in nitrogen plasma flows *J. Thermophys. Heat Transfer* **14** 489–95
[61] Caz A T-del *et al* 2019 The lisbon kinetics Boltzmann solver *Plasma Sources Sci. Technol.* **28** 043001
[62] Caz A T-del, Guerra V, Pinhão N, Pintassilgo C D and Alves L L 2021 On the quasi-stationary approach to solve the electron Boltzmann equation in pulsed plasmas *Plasma Sources Sci. Technol.* **30** 065008
[63] Pitchford L C *et al* 2017 Lxcat: an open-access, web-based platform for data needed for modeling low temperature plasmas *Plasma Process. Polym.* **14** 1600098
[64] Pancheshnyi S, Biagi S, Bordage M C, Hagelaar G, Morgan W, Phelps A and Pitchford L C 2012 The lxcat project: electron scattering cross sections and swarm parameters for low temperature plasma modeling *Chem. Phys.* **398** 148–53
[65] Carbone E, Graef W, Hagelaar G, Boer D, Hopkins M M, Stephens J C, Yee B T, Pancheshnyi S, Van Dijk J and Pitchford L 2021 Data needs for modeling low-temperature

non-equilibrium plasmas: the lxcat project, history, perspectives and a tutorial *Atoms* **9** 16
[66] Likhanskii A V, Shneider M N, Macheret S O and Miles R B 2007 Modeling of dielectric barrier discharge plasma actuators driven by repetitive nanosecond pulses *Phys. Plasmas* **14** 073501
[67] Xu S, Cai J and Li J 2016 Modeling and simulation of plasma gas flow driven by a single nanosecond-pulsed dielectric barrier discharge *Phys. Plasmas* **23** 103510
[68] Herron J T 2001 Modeling studies of the formation and destruction of no in pulsed barrier discharges in nitrogen and air *Plasma Chem. Plasma Process.* **21** 581–609
[69] Pintassilgo C, Guaitella O and Rousseau A 2009 Heavy species kinetics in low-pressure dc pulsed discharges in air *Plasma Sources Sci. Technol.* **18** 025005
[70] Loureiro J and Ferreira C 1986 Coupled electron energy and vibrational distribution functions in stationary N_2 discharges *J. Phys. D: Appl. Phys.* **19** 17
[71] Shkurenkov I, Burnette D, Lempert W R and Adamovich I V 2014 Kinetics of excited states and radicals in a nanosecond pulse discharge and afterglow in nitrogen and air *Plasma Sources Sci. Technol.* **23** 065003
[72] Wormeester G, Pancheshnyi S, Luque A, Nijdam S and Ebert U 2010 Probing photo-ionization: simulations of positive streamers in varying N_2: O_2-mixtures *J. Phys. D: Appl. Phys.* **43** 505201
[73] Li Y, Fu Y, Liu Z, Li H, Wang P, Luo H, Zou X and Wang X 2023 Effect of photoionisation on initial discharge in air under nanosecond pulse voltage *High Voltage* **8** 340–6
[74] Capitelli M, Ferreira C M, Gordiets B F and Osipov A I 2013 *Plasma Kinetics in Atmospheric Gases* vol 31 (Springer)
[75] Van Gaens W and Bogaerts A 2013 Kinetic modelling for an atmospheric pressure argon plasma jet in humid air *J. Phys. D: Appl. Phys.* **46** 275201
[76] Dias T C and Guerra V 2025 Are local-field and local-energy approximations appropriate for modeling nanosecond discharges? *J. Phys. D: Appl. Phys.* **58** 185204
[77] Peng Y, Chen X, Deng Y, Lan L, Zhan H, Pei X, Chen J, Yuan Y and Wen X 2022 Kinetic study of key species and reactions of atmospheric pressure pulsed corona discharge in humid air *Plasma Sci. Technol.* **24** 055404